

Stress dependence of the magnetic
properties of steels

by

Michael Kenneth Devine

A Thesis Submitted to the
Graduate Faculty in Partial Fulfillment of the
Requirements for the Degree of
MASTER OF SCIENCE

Department: Materials Science and Engineering
Major: Metallurgy

Approved:

Signature redacted for privacy

In Charge of Major Work

For the Major Department

For the Graduate College

Iowa State University
Ames, Iowa

1992

TABLE OF CONTENTS

	Page
CHAPTER 1. INTRODUCTION	1
Origin of Ferromagnetism	3
Influence of Microstructure and Composition	5
Influence of Stress	11
NDE Applications	28
Statement of Problem and Experimental Approach	29
 CHAPTER 2. EXPERIMENTAL PROCEDURE FOR MAGNETIC MEASUREMENTS	30
Magnescope Instrumentation	30
Inspection Head Design	32
 CHAPTER 3. LABORATORY SCALE STRESS DETECTION WITH A SOLENOID	37
Introduction	37
Materials and Experimental Procedure	37
Results and Discussion	38
Conclusions	45
 CHAPTER 4. APPLIED STRESS MEASUREMENT USING INSPECTION HEAD	49
Introduction	49
Materials and Experimental Procedure	49
Results and Discussion	52
Conclusions	69

CHAPTER 5. COMPARISON BETWEEN LABORATORY AND RAIL COMPONENTS	70
Introduction	70
Materials and Experimental Procedure	70
Results and Discussion	71
Conclusions	74
CHAPTER 6. APPLIED STRESS MEASUREMENTS IN RAILROAD RAIL .	77
Introduction	77
Materials and Experimental Procedure	77
Results and Discussion	78
Conclusions	89
CHAPTER 7. CONCLUSIONS	91
REFERENCES	94
ACKNOWLEDGEMENTS	96
APPENDIX (Data for Parameter Plots)	98

CHAPTER 1. INTRODUCTION

It is well known that the magnetic properties of ferromagnetic materials are sensitive to microstructural and mechanical changes. Variations in applied stress, composition, and geometry will, either alone or in combination with each other, cause the magnetization process to change. The primary way to monitor changes in the magnetization process is to run the material or component of interest through a hysteresis cycle and plot the magnetic response on the B, H (magnetic induction, magnetic field) plane. The result is a hysteresis loop, a typical example of which is given in Figure 1.1. The figure also shows a number of parameters that are used to describe the hysteresis loop. The coercivity (H_c) is the magnetic field value as the induction passes through zero. The remanence (B_r) is the induction value as the magnetic field passes through zero. The maximum differential permeability (μ'_{\max}) is the slope of the loop as it passes through the coercivity. The hysteresis loss (W_h) is the area enclosed by the loop. The initial differential permeability (μ'_{in}) is the slope of the curve just at the start of magnetization from the demagnetized condition. The maximum or saturation induction (B_{\max}) is the largest induction value.

It is useful to be able to monitor the magnetic changes in materials as external conditions vary. This is especially true for circumstances where the material is exposed to

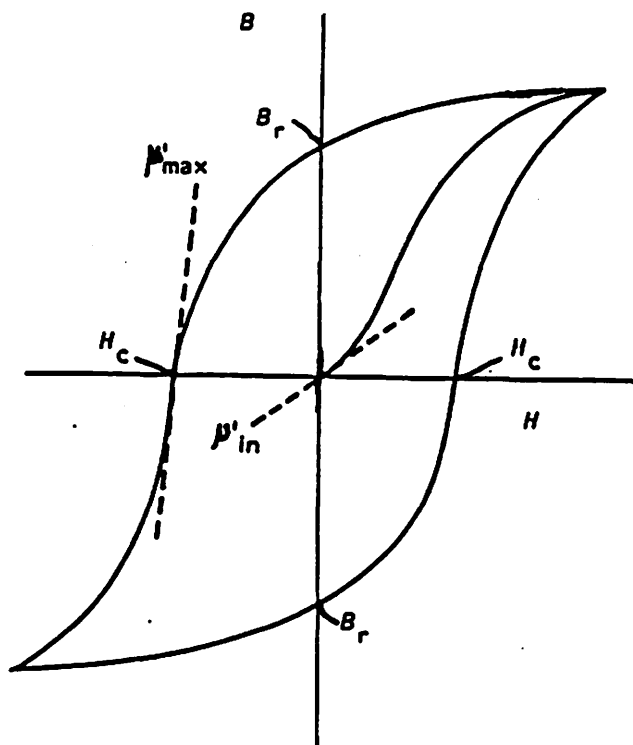


Figure 1.1: Example of a typical hysteresis loop
 H_c = Coercivity, B_r = Remanence
 μ'_{in} = initial differential permeability
 μ'_{max} = maximum differential permeability

situations where it may fail. The potential exists for on-line monitoring of a component in service or as a quality control tool for material suppliers. Magnetic testing may be able to meet present day needs for NDT of steel components.

Origin of Ferromagnetism

Ferromagnetism arises from the electronic magnetic moments in a material becoming ordered into small regions called domains. Each domain is made up of typically 10^{12} to 10^{18} magnetic moments aligned in one direction. The region between domains, where the magnetic moments change their orientation, is called a domain wall. A schematic of a domain wall is given in Figure 1.2. The change in orientation happens gradually, over several hundred atom layers, due to energy considerations. Every domain is magnetized to saturation but unless a majority of them are aligned in a particular direction, the vector sum of all the domains will be zero and the material is considered to be macroscopically demagnetized. The direction of alignment for domains generally follows one of the crystallographic axes with certain axes preferred over others because of magnetocrystalline anisotropy, these are called the "easy axes". The atomic ordering in these directions allows for a reduction in energy, referred to as the magnetocrystalline anisotropy energy. A magnetic material

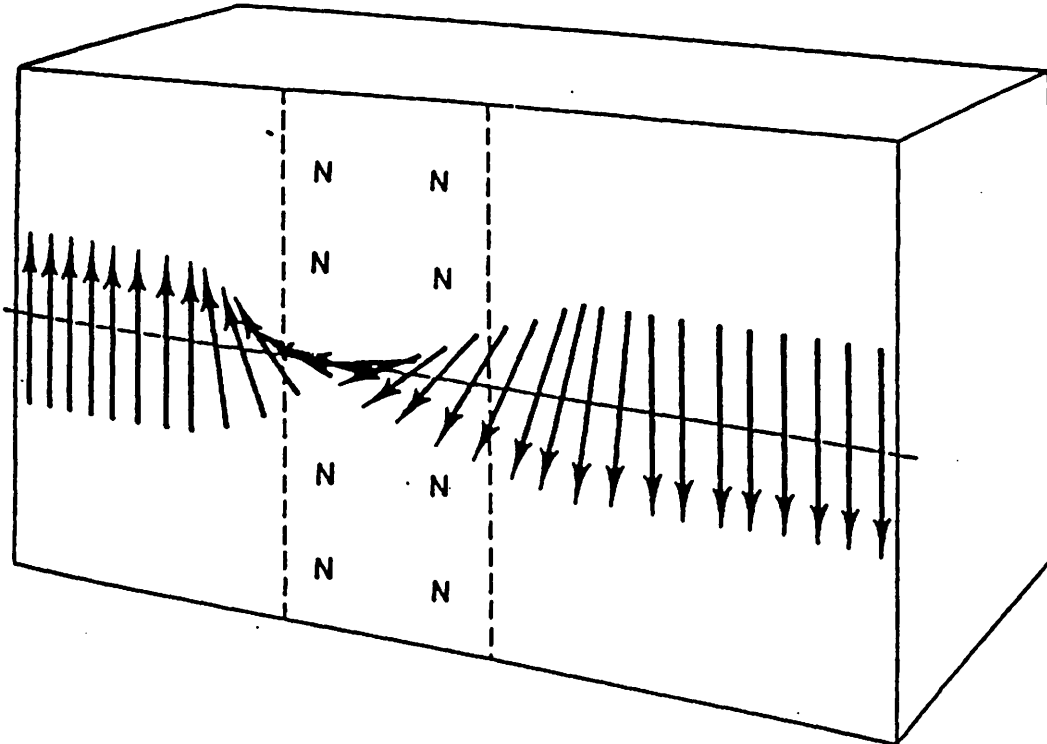


Figure 1.2: Schematic of orientation change of magnetic moments in a domain wall

that is not macroscopically magnetized contains many domains because the existence of a single domain is normally energetically unfavorable. A domain's energy (called the magnetostatic energy) is increased as the number of magnetic moments is increased. When the magnetostatic energy exceeds the energy required for domain wall formation, multiple domains form.

When a magnetic field is applied, domains favorably aligned with the field tend to grow at the expense of the unfavorably aligned domains. The growth of a domain is accomplished through motion of domain walls. The amount of growth, or the distance a domain wall will travel, depends on the strength and direction of the applied magnetic field. The microstructure, composition and existence of stress in the solid, will also affect domain growth.

Influence of Microstructure and Composition

This section deals with changes in the magnetic response of ferromagnetic materials due to microstructure and composition. This includes factors such as voids, cracks, non-ferromagnetic inclusions, or impurities which affect the mobility of domain walls during magnetization. The mobility is affected for two reasons; one, the energy of the domain wall is reduced by the nonmagnetic region; two, the production

of subsidiary or spike domains on the nonmagnetic region which alter the magnetostatic energy of the domain.

The energy of a domain can be reduced by an inclusion because the domain wall area is diminished and the wall's surface energy is reduced. The wall is then inhibited from moving further until the applied magnetic field supplies enough energy to push it past the region.

The production of subsidiary domains or free poles around inclusions was theorized by Néel (1). The free poles produce a significant restoring force on a domain wall. According to Néel, an inclusion that is entirely within a domain have free poles around it (see Figure 1.3) with an associated demagnetization energy. As a domain wall bisects the inclusion, the free poles are redistributed according to the domain orientation and the magnetostatic energy is reduced. In addition, subsidiary spike domains may form on the inclusion, further reducing the magnetostatic energy. The energy could be reduced to zero because closure domains would form. Néel's theory has been confirmed by Williams (2, 3) who studied the surface domain structure in an iron-silicon crystal and found the existence of spike domains.

The influence of inclusions on inhibiting domain wall movement is dependent on the size of the inclusion. A large inclusion (>1 micron, or approximately the domain wall thickness) impedes walls primarily through formation and

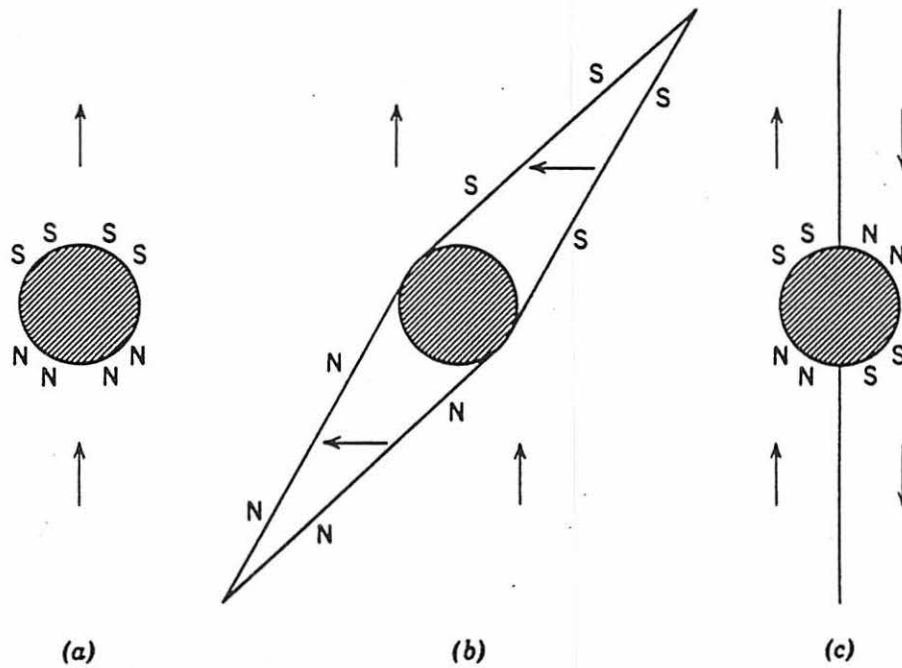


Figure 1.3: a) Spherical inclusion within a domain
 b) Free pole distribution as a domain wall attempts to pass through the inclusion
 c) Domain structure as the domain wall bisects the inclusion

growth of spike domains. Small inclusions hinder a wall primarily through reduction of domain wall energy. Naturally, in most microstructures the inclusion sizes vary widely and both influences will determine the magnetic behavior at the macroscopic level. This complexity makes it difficult to predict how the magnetic parameters will change. However, the effects of specific types of inclusions on the magnetic hysteresis parameters can be studied and good estimations of the mechanisms can be made.

Large non-magnetic regions in a ferromagnetic material will tend to increase the coercivity and reduce the initial differential permeability through increases in the magnetostatic energy. Small non-magnetic phases, such as second-phase precipitates or carbide inclusions will tend to also increase the coercivity and initial differential permeability by reducing the surface energy of the domain walls.

Previous work

Two comprehensive reviews of composition effects on magnetic properties have been published. One has been done by Bozorth (4) while a more recent review has been done by Chin and Wernick (5).

Jiles (6) found that increasing carbon content in plain carbon steels increased the coercivity and hysteresis loss and decreased the initial differential permeability. These

effects were attributed to the increased pinning of the domain walls by carbide particles. The presence of nonmagnetic phases played an additional role in the magnetic response. Specimens with a lamellar carbide network had a higher coercivity than specimens with spheroidized carbides. The lamellae provided stronger pinning sites which inhibited domain wall motion. The carbon content changes did not appear to affect the remanence or maximum differential permeability.

In a study of the different microstructures produced by various heat treatments of AISI 4130, Jiles (7) found that of the three microstructures produced (pearlite, bainite, and martensite) the pearlitic microstructure had the smallest coercivities, smallest hysteresis losses and largest initial differential permeabilities. The martensite had the largest coercivities, largest hysteresis losses and smallest initial differential permeabilities. The bainite group had intermediate values for all three parameters. Similar effects were seen in a study of AISI 4140 steels by Jiles (8).

Gorkunov and Batukhtina (9) investigated the variation of remanence and maximum induction with tempering. They found that the remanence and maximum induction varied throughout a tempering cycle, corresponding to changes in the microstructure at those points. In a later, similar study, Gorkunov et al. (10) found variations in the initial differential permeability and maximum differential permeability.

A number of researchers (11) have found a relationship between coercivity and dislocation density. They found that $H_c \approx k\sqrt{N}$ where k is a scaling constant and N is the dislocation density. This relation is not universal though, because its simplicity does not take into account the structure and distribution of the dislocations (such as those at grain boundaries).

Jiles (8) found the coercivity decreased with increasing compressive plastic strain from 0 to 10% in AISI 4140 samples. The amount of decrease depended on the microstructure present. The samples with a martensitic structure decreased the most while the pearlitic samples changed the least. The remanence, maximum differential permeability and initial differential permeability increased sharply for all microstructures going from 0 to 2% compressive plastic strain but varied little with strain above 2% deformation.

Kwun and Burkhardt (12) found little change in the magnetic properties due to changing grain size in samples of AISI 4340. This is surprising because it would be expected that the larger number of dislocations associated with smaller grains would influence the magnetic properties somewhat. It is possible that they did not examine a large enough spread of grain sizes. Jiles (6) reported that the grain size is not the dominant microstructural factor once the carbon content gets beyond 0.2 wt%.

Thompson et al. (13) studied the variation of the coercivity and maximum differential permeability in the heat affected zone, base, and weldments in pearlitic steel weldings. The coercivity was larger in the weld metal compared with the base metal. The maximum differential permeability was smaller in the weld metal than the parent metal. Electron microscopy revealed an increased concentration of second phase lamellae in the weld metal. This led to an increased pinning of the domain walls, increasing the coercivity and reducing the permeability.

In conclusion, it can be seen that composition and microstructural variations such as alloy content, presence of nonmagnetic phases and dislocations affect the magnetic properties. No single factor controls the magnetic response, rather it is the combination of influences.

Influence of Stress

The effect of stress on ferromagnetic materials is complicated, there are a number of factors which must be considered. One factor is whether the stress is within the elastic range of the material or whether it has exceeded this limit and is plastically deforming the material. Also, one must consider if the material has a positive or negative magnetostriction. The direction of stress with respect to the

domain is important along with the possibility of multiple stresses acting simultaneously.

Magnetostriction refers to the change in dimensions in ferromagnetic materials as they are magnetized. The change in dimensions is small for most ferrous materials and depends on the strength and orientation of the applied magnetic field. Magnetostriction is thought to come about from the strain dependence of anisotropy resulting from electron spin-orbit coupling. The electrons in an atom have an orbit that is noncircular. They are also distributed nonspherically around the nucleus as represented in Figure 1.4. The arrows depict the direction of the individual magnetic moments. The top row depicts the arrangement while the material is above the Curie temperature, with the magnetic moments randomly distributed. As the temperature is decreased and passes through the Curie point, there is an ordering when the material becomes ferromagnetic (as shown in the second row). This produces a spontaneous magnetostriction (even though there is no applied field) as the spins align along a specific direction within domains, dependent on the crystal anisotropy. As a magnetic field is applied, further reorientation occurs due to the effect of the field on the electron spins (as shown in the third row).

A material with a positive magnetostriction increases in length along the magnetization direction. Conversely, a material with a negative magnetostriction will decrease in

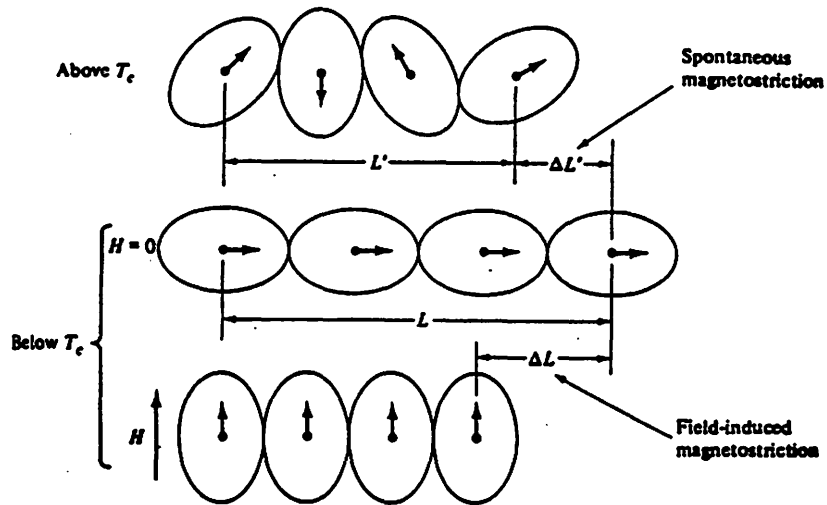


Figure 1.4: Orientation of magnetic moments showing origins of magnetostriction as temperature is reduced from the Curie point

length in the direction of magnetization. Magnetostriction plays a major role in determining the response of a ferromagnetic material to stress. A tensile stress applied to a material that has a positive magnetostriction can increase the magnetic induction. The stress produces an effective magnetic field that acts in conjunction with any applied magnetic field. The effective field will be described below.

Most ferrous alloys have a mixed magnetostriction depending on the applied magnetic field and stress. Under zero stress, iron has a positive magnetostriction up to about 250 Oe, above this it has a negative magnetostriction. The point at which iron changes from positive to negative magnetostriction is called the Villari reversal. The Villari reversal point changes with stress and composition of the material.

In order to consider the effect of stress on the magnetization of materials, one must go into further detail into domain walls and domain structure. As mentioned earlier, a domain wall is the transition region between two domains where the orientation of the moments change from that in one domain to the other. The change is gradual, occurring over a few hundred atom layers. The number of layers involved in the orientation change is called the domain wall thickness. There are two competing forces which determine the domain wall thickness, one arising from the exchange energy, the other from the anisotropy energy.

The exchange energy arises from the interaction between magnetic moments and can be expressed by,

$$E_{ex} = -\mu_0 z J m_i m_j \cos\phi \quad (1)$$

where μ_0 is the permeability of free space, z is the number of nearest neighbors, m_i , m_j are the strength of the magnetic moments (usually $m_i = m_j = m$) and ϕ is the angle between the neighboring moments.

In the simple case of a linear chain, each moment has two nearest neighbors ($z = 2$). If ϕ is small, one can substitute $\cos\phi = 1 - \phi^2/2$ and equation (1) simplifies to

$$E_{ex} = \mu_0 J m^2 (\phi^2 - 2) \quad (2)$$

Summing the individual exchange energies over the number of moments in the wall:

$$E_{ex} = \mu_0 J m^2 \phi^2 n \quad (3)$$

where n is the number of moments in the wall.

If we consider a 180° domain wall in a lattice with lattice parameter a , ϕ becomes π/na and substituting into (3)

$$E_{ex} = \mu_0 J m^2 \pi^2 / na^2 \quad (4)$$

one can see that the larger n is, the lower the value of ϕ and the lower the exchange energy. This corresponds to a wide domain wall.

Anisotropy energy is associated with the energy differences of the magnetic moments when they are aligned along different crystallographic directions. In the case of a domain wall of thickness l_d , it can be expressed as:

$$E_{ani} = K l_d \quad (5)$$

where k is the anisotropy constant. Equation (5) is minimized for a thin wall.

The summation of (4) and (5) provides an expression for the domain wall energy,

$$E_{tot} = E_{ex} + E_{ani} \quad (6)$$

or

$$E_{tot} = (\mu_0 J m^2 \pi^2 / l_d a) + K l_d \quad (7)$$

Depending on which term is dominant, the energy can be minimized by a small l_d (through anisotropy energy) or by a large l_d (through exchange energy). Table 1.1 lists approximate domain wall thicknesses for some ferromagnetic materials. As can be seen, the material with the largest anisotropy energy, cobalt has the thinnest domain wall.

Nickel has the smallest anisotropy energy and has the thickest domain wall of the group.

There are two types of domain walls, 180° and non-180°. The 180° domain walls are the most common and occur between anti-parallel domains (oriented 180° apart, hence the name). The non-180° domain walls have orientations depending on the direction of the easy axes in the material. For example, in iron the easy axes are the <100> directions so the domain

Table 1.1: Various domain wall properties

	Fe	Co	Ni
Domain wall thickness in nanometers	40	15	100
in lattice parameters	138	36	285
Exchange energy (J)	2.5×10^{-21}	N/A	3.2×10^{-21}
Anisotropy energy (at 300K, J/m ³)	4.8×10^4	45×10^4	-5.7×10^4

walls between a domain oriented in the (010) direction and one oriented in the (001) direction would be called a 90° domain wall. In nickel, the easy axes are the <111> directions so the non-180° domain walls will be either 71° or 109°.

The 180° and non-180° domain walls respond differently to stress. The 180° walls are not greatly affected by stress (28) because the energy of a particular domain orientation is reduced by an applied stress, the energy in the anti-parallel domain direction is reduced by the same amount. The net

result is no favored orientation and no domain wall movement. Since 90° walls are not separating anti-parallel domains there is a favored orientation and some domain growth is accomplished through wall movement under the action of stress. The stress produces an effective magnetic field, H_e , which can be expressed

$$H_e = 3\lambda_s \sigma / 2\mu_0 M_s \quad (8)$$

where λ_s is the magnetostriction when the material is at the saturation magnetization, σ is the applied stress, μ_0 is the permeability of free space and M_s is the saturation magnetization. This effective magnetic field gives rise to a change in magnetization. The result of all this is that the 180° domain walls give no contribution to magnetostriction since they do not move with stress while 90° domain walls give a significant contribution.

Modelling work

Much work has been done in mathematically modelling the hysteresis curves over the past couple of decades. However, most models that have been presented have only been of limited use and limited success. Stoner and Wohlfarth (14) were one of the first but their model applies mainly to single domain particles. The Preisach (15) model is useful for modelling

the recording process because it produces a rectangular hysteresis curve. More recently, the Jiles-Atherton model (16) has been used for general hysteresis modelling. It is capable of modelling the macroscopic hysteresis loops without the limitations of single domain particles or rectangular hysteresis loops.

The Jiles-Atherton model uses a modified Langevin function for describing the anhysteretic curve and two differential equations that represent irreversible differential permeability and reversible differential permeability.

The calculation of the irreversible differential susceptibility begins with an equation for the energy lost to pinning,

$$E_{\text{pin}}(M_{\text{irr}}) = n \langle \epsilon_p \rangle \int dM_{\text{irr}} \quad (9)$$

where n is the number density of pinning sites, $\langle \epsilon_p \rangle$ is the average pinning energy for 180° domain walls, m is the magnetic moment of a typical domain and M_{irr} is the irreversible magnetization component.

The three variables in front of the integral can be bundled into one,

$$\mu_0 k = \frac{n \langle \epsilon_p \rangle}{2m} \quad (10)$$

and rewriting (9)

$$E_{pin}(M_{irr}) = \mu_0 k \int dM_{irr} \quad (11)$$

Reference (16) describes how equation (11) can be used to derive the hysteresis equation for irreversible changes in magnetization as,

$$M_{irr} = M_{an} - k \delta (dM_{irr} / dH_e) \quad (12)$$

H_e is an effective field,

$$H_e = H + \alpha M \quad (13)$$

and δ is a directional parameter dependent on temporal change in H . It has the value +1 for positive increments of dH/dt and -1 for negative increments of dH/dt .

Rearranging equation (12) to give the equation for irreversible differential susceptibility,

$$\begin{aligned} \chi_{irr} &= dM_{irr} / dH \\ &= (M_{an} - M_{irr}) / k \delta - \alpha(M_{an} - M_{irr}) \end{aligned} \quad (14)$$

The reversible differential susceptibility is dependent on the component of reversible magnetization which can be represented as the displacement between the prevailing

irreversible magnetization and the anhysteretic magnetization at a given field strength

$$M_{rev} = c (M_{an} - M_{irr}) \quad (15)$$

where c is a constant which describes the rigidity of the domain walls. If we differentiate equation (14) with respect to H we find,

$$dM_{rev} / dH = c (dM_{an}/dH - dM_{irr}/dH) \quad (16)$$

The total differential susceptibility can then be represented as the summation of the irreversible and reversible components

$$\begin{aligned} dM/dH &= dM_{irr}/dH + dM_{rev}/dH \\ &= (1 - c) \frac{M_{an} - M_{irr}}{k\delta - \alpha(M_{an} - M_{irr})} + c (dM_{irr}/dH) \end{aligned} \quad (17)$$

Figure 1.5 shows a theoretical hysteresis loop obtained through equation (17) with $M_s = 1.7 \times 10^6$ A/m, $a = 1000$ A/m, $k = 2000$ A/m, $\alpha = 0.001$ and $c = 0.1$. To include the effects of stress, Sablik (17) introduced the equivalent magnetic field, H_σ , which results from interaction of the stress with the magnetostriction,

$$H_\sigma = (3\sigma / 2\mu_0) * (\partial\lambda / \partial M)_T \quad (18)$$

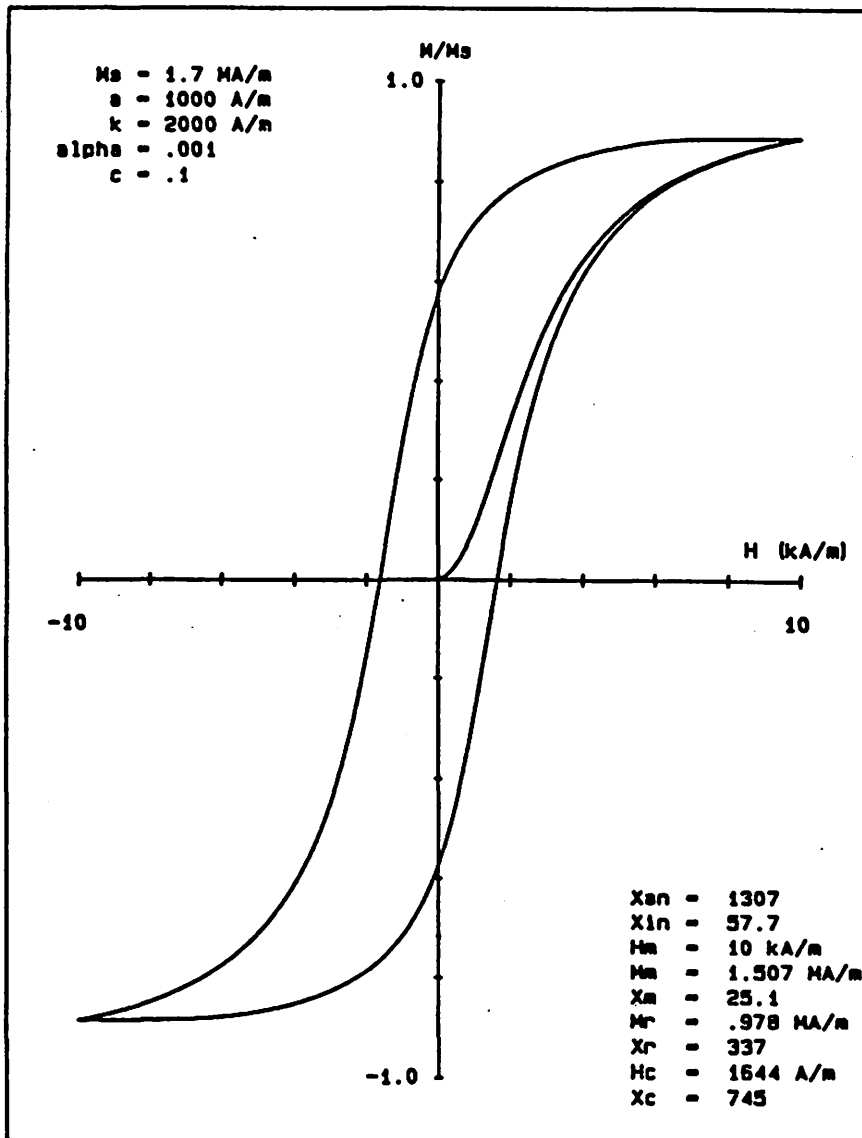


Figure 1.5: Theoretical hysteresis loop obtained through equation (17) with $M_s = 1.7 \times 10^6 \text{ A/m}$, $a = 1000 \text{ A/m}$, $k = 2000 \text{ A/m}$, $\alpha = 0.001$ and $c = 0.1$

where λ is the bulk magnetostriction and σ is the applied stress. In (19) Garikepeti extended Sablik's work to derive a relationship between the anhysteretic differential permeability at low fields and stress,

$$[\chi'_{am}(\sigma)]_{H=0} = M_s / (3\alpha - (\alpha + 3b\sigma/\mu\sigma)M_s) \quad (19)$$

which can be rewritten as,

$$1/[\chi'_{am}(0)]_{H=0} - 1/[\chi'_{am}(\sigma)]_{H=0} = 3b\sigma/\mu\sigma \quad (20)$$

Experiments on samples of AISI 4130 have demonstrated excellent agreement.

Subsequent work

Pitman (18) reported on the changes in the hysteresis parameters under uniaxial stresses ranging from -400 MPa to +400 MPa in a steel specimen (exact composition was not specified). It was found that tensile stress up to 100 MPa increased the initial differential permeability and remanence while compressive stress reversed these trends. The steel specimen was magnetostrictively positive in the stress ranges tested. The remanence reached a maximum at 100 MPa after which it decreased slightly as the stress was increased. This

was attributed to the Villari reversal. Under compressive stress the remanence decreased significantly and continuously.

Garikepati et al. (19) reported that in AISI 4130, the inverse of the anhysteretic differential permeability varied monotonically with stress between -300 MPa and +300 MPa. They were able to express the relationship between stress and the anhysteretic permeability at the origin as

$$1 / [\chi'_{am}(\sigma)]_{H=0} = 2.95 \times 10^{-3} - (5.73 \times 10^{-12}) \sigma . \quad (21)$$

Langman (20) found that mechanical stress can cause the magnetic flux density and magnetic field strength to become non-parallel. He used an innovative technique involving a device called the "rotation rig" to measure the change in direction of the magnetic field under bending stresses, either in the elastic or plastic range. The rotation rig measured the magnetic induction parallel and perpendicular to an applied bending stress. By monitoring the ratio of induction-parallel and induction-perpendicular to the stress one can measure the applied stress. The technique gives the same reading for a given stress, regardless of whether it is compressive or tensile.

In another paper, Langman (21) reported plastic bending tests performed on medium carbon steels. The rotation rig was able to measure the difference in principal stresses and their directions in an annealed specimen subjected to small elastic

stresses. Results were also presented on a previously annealed steel bar stressed in a four-point bending test beyond the yield stress. The rotation rig measurements tracked the stress in the bar up to yielding after which the measurements reversed their trend. After the load was reduced to zero, the rotation rig measurements did show the residual plastic stress left in the bar.

Kwun and Burkhardt (12) reported on stress effects on the hysteresis loops of AISI 410 stainless steel and SAE 4340 steel specimens. They took magnetic measurements with a technique similar to the one used in the present work. They found the shape and magnitude of the hysteresis loops changed significantly with stress. In most cases the maximum induction increased with increasing tension. Some of the specimens of the 410 stainless showed a peak in the maximum induction at 20 ksi after which it decreased. They also found that the ratio of the remanence over the maximum induction increased under increasing tension and decreased under increasing compression.

Jiles et al. (22) studied the elastic tensile response of some nickel specimens. It was found in annealed specimens that there was a large decrease in initial differential permeability and a slight increase in coercivity. However, after cold working, the H_c and μ'_m became relatively insensitive to elastic stresses. This was a consequence of

the numerous dislocations introduced from the plastic deformation.

Langman (23) performed experiments on low carbon steels undergoing uniaxial and biaxial stress in both tension and compression. The uniaxial test had stress and magnetization directions parallel. The biaxial test had $\sigma_x = \sigma_y$ with magnetization parallel to σ_x . Uniaxial stress in the tensile direction had little effect on the coercivity. Biaxial tensile stress caused the coercivity to decrease slightly as the stress was increased. The remanence, maximum differential permeability and the maximum induction increased with increasing uniaxial tension up till about 40 MPa (5800 psi) after which they decreased with increasing tension. At maximum tensile stress B_r , μ'_{max} , and B_{max} were below their zero stress values. Under increasing biaxial tension, B_r , μ'_{max} , and B_{max} all decreased, there was no initial increase. Under uniaxial compression, H_c , B_r , μ'_{max} , and B_{max} all decreased, with μ'_{max} and B_r showing increased sensitivity to the stress changes. Biaxial compression had the same effect as uniaxial compression, all the parameters decreased. However, the decrease under biaxial compression was greater than that under uniaxial compression.

The increased sensitivity of the hysteresis parameters to biaxial stress was due to the greater number of 90° domain walls that were affected. Figure 1.6 illustrates an element

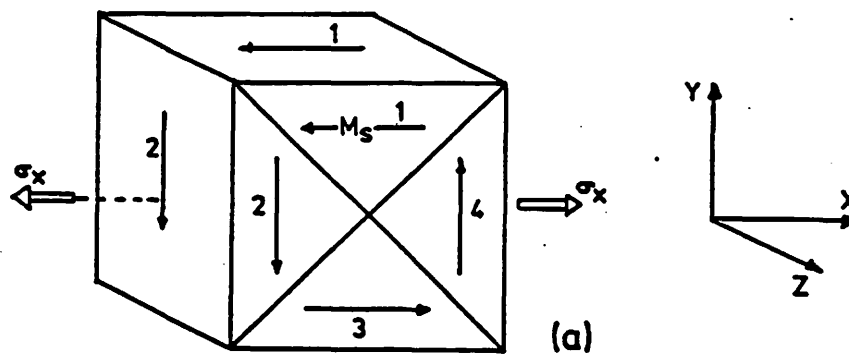


Figure 1.6: Element of a magnetic material with four domains aligned along the crystal axes, separated by 90° walls

of the sample showing four domains aligned along the crystal axes and separated by 90° domain walls. Under uniaxial tensile stress, the magnetoelastic energy of domains 1 and 3 were reduced because they are parallel to the stress. The magnetoelastic energy of domains 2 and 4 do not change because they are aligned perpendicular to the stress. Domains 1 and 3 will then grow at the expense of domains 2 and 4. In the case of biaxial tension, all the domains are aligned favorably with some stress and all will grow (in the z direction). The increased domain activity explains the increased sensitivity of the hysteresis parameters to biaxial stress.

NDE Applications

The potential of magnetic hysteresis measurements for NDE applications is evident from the above discussion. Sanford-Francis (24, 25) reported on a number of inspections performed on failed components including axles from aircraft. Measurements of the magnetic permeability decreased noticeably between an unfailed portion and a failed portion probably because of a buildup of dislocations which impede domain wall motion. Numerous other examples were mentioned. It was found that the permeability correlated well with hardness and thus could be used to determine if a component had undergone excessive work hardening during service and needed to be removed.

Bussièrè (26) mentioned a number of on-line measurements that can be implemented using the magnetic hysteresis technique, including measuring the carbon content and estimating the ultimate tensile strength of killed and rimmed carbon steel castings.

In conclusion, while there has been some activity at utilizing magnetic hysteresis techniques for NDE applications, it has not yet been fully explored. There are many applications, such as stress detection that need further research.

Statement of Problem and Experimental Approach

The purpose of this work was to develop an in situ magnetic hysteresis measurement technique for monitoring applied stresses in structural components. Stress measurements were first made by wrapping samples with a flux coil and magnetizing with a solenoid. Next, stress measurements were made using an in situ measurement technique under laboratory conditions. Then structural components of similar metallurgy to the laboratory specimens were measured to confirm that laboratory measurements corresponded to field measurements. Finally, stress tests were performed on industrial components.

CHAPTER 2. EXPERIMENTAL PROCEDURE FOR MAGNETIC MEASUREMENTS

Magnescope Instrumentation

Two instruments were used to make the magnetic measurements: a portable unit called the Magnescope (30) and a non-portable, lab based hysteresisgraph unit. The Magnescope is a portable magnetic inspection device consisting of an inspection head, gaussmeter, fluxmeter, bipolar power supply, personal computer, control/data acquisition system and software. The components of the Magnescope are contained in a protective box for portability. The lab based hysteresisgraph unit consists of the same components as the Magnescope but contained in a non-portable lab rack. A block diagram (31) showing the arrangement of the components is given in Figure 2.1. The gaussmeter and fluxmeter are used for measuring the magnetic field and flux density. The bipolar power supply is used to generate the field through the inspection head and is fully programmable by the personal computer. The computer also monitors the output of the gaussmeter and fluxmeter. The software is capable of analyzing the output from the meters and presents the magnetic hysteresis parameters almost immediately after an inspection.

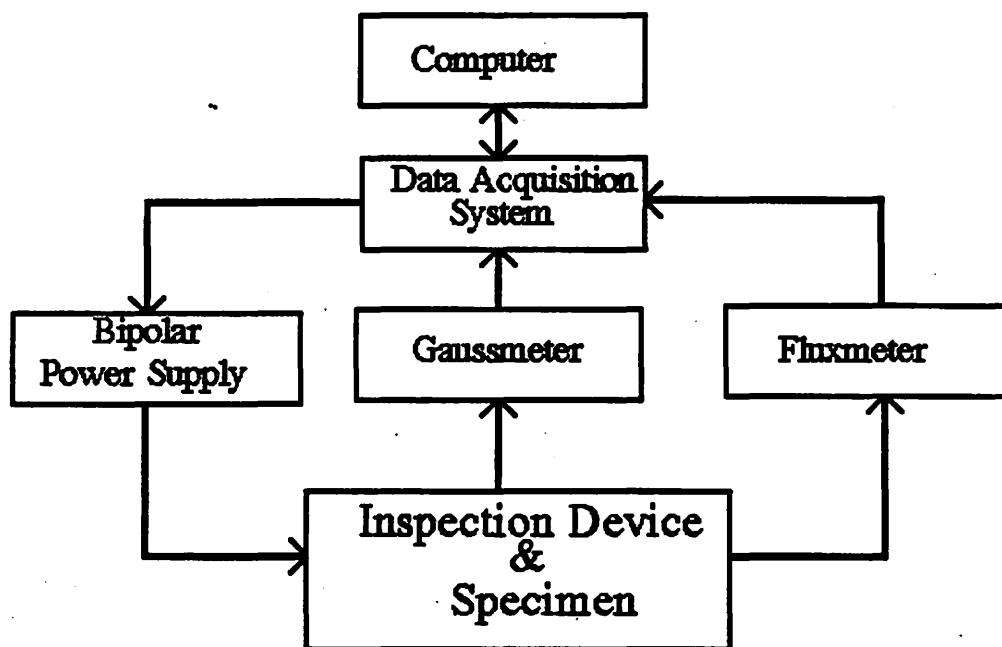


Figure 2.1: Block diagram of the Magnescop

Inspection Head Design

An inspection head typically consisted of a C-shaped soft iron electromagnet, with a flux coil to measure the flux density. The magnetic field strength was measured by a Hall sensor, positioned on the surface of the specimen being investigated. A schematic of an inspection head on a specimen is given in Figure 2.2. The type of inspection head used with the Magnescope depends on the geometry of the sample to be inspected. Two factors that vary from one inspection head to another are the size and cross sectional area of the C-core. Sometimes the pole pieces are machined to match the curvature of a specimen.

The inspection head used to perform the measurements reported here had flat pole pieces with the following dimensions:

Cross sectional area of C-core: 2.5 x 2.5 cm (1 x 1 in)

Path length in C-core: 12.7 cm (5 in)

When an inspection head is placed on a specimen for a measurement, a magnetic circuit consisting of the C-core and the specimen material between the pole pieces is obtained. The magnetic flux path follows the direction shown in Figure 2.3, although this is somewhat arbitrary because the depth of penetration (also called the skin depth) is dependent on the magnetic permeability of the material and the frequency of the

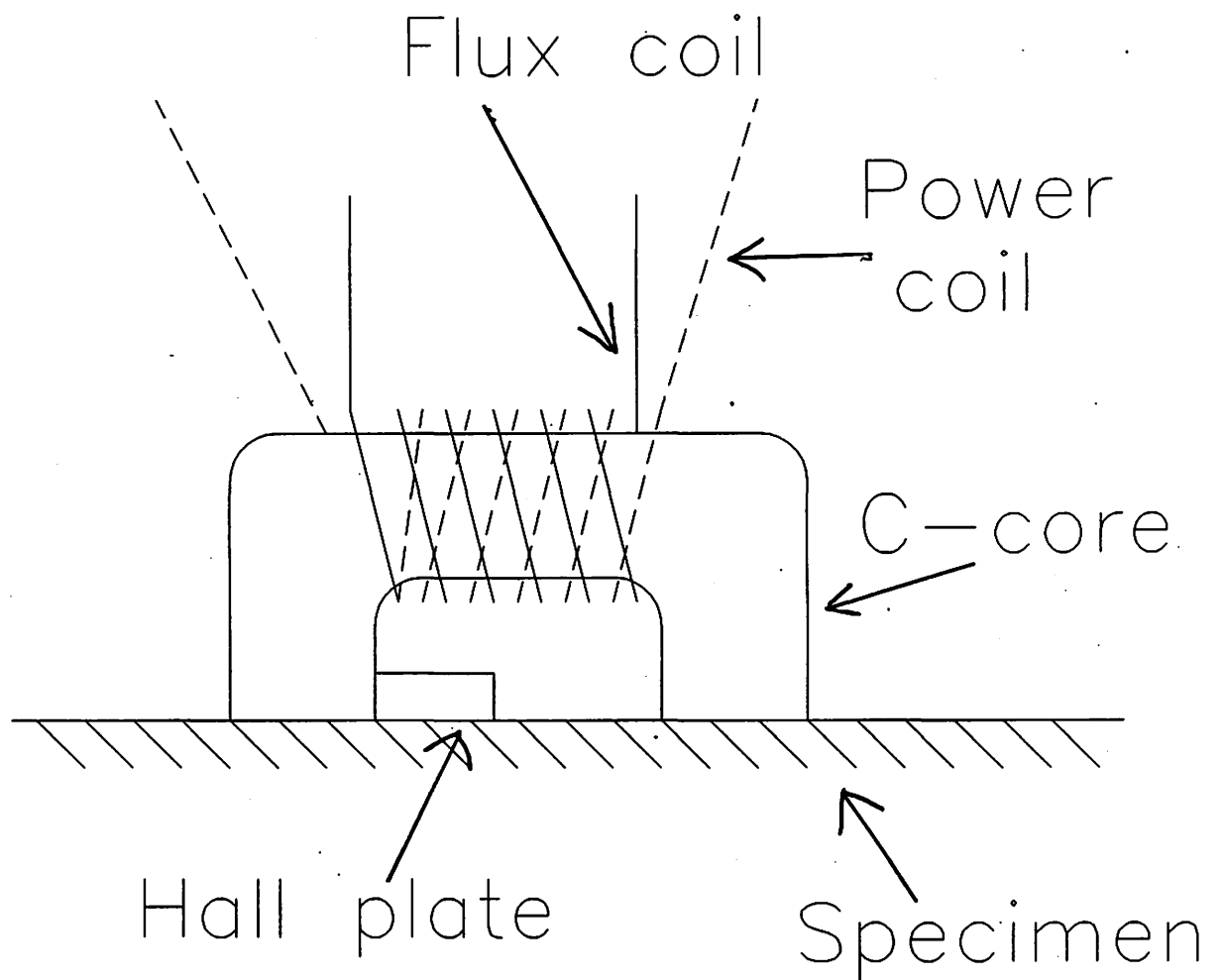


Figure 2.2: Components of an inspection head

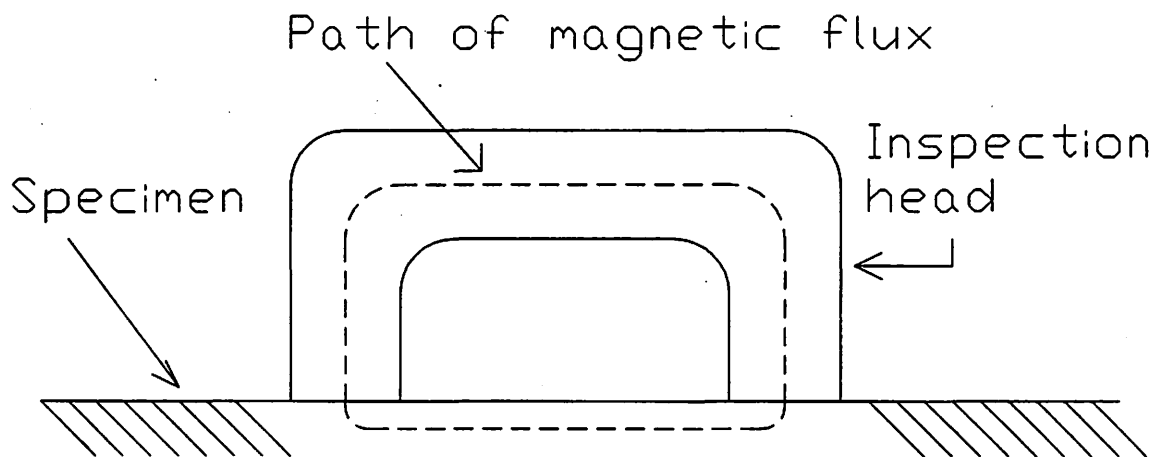


Figure 2.3: Schematic of the flux path in the magnetic circuit created when inspection head is placed on a sample

hysteresis cycle. The permeability of steels varies widely and no attempt was made at quantifying it for skin depth calculations. The frequency of the hysteresis cycle is fixed at 0.01 Hz. The average depth of penetration has been estimated to be 0.64 cm (0.25 in).

The magnetic hysteresis technique is based on the assumption that changes in the specimen will alter the magnetic flux path which will be picked up by the flux coil on the C-core. This eliminates the step of wrapping a flux coil around the specimen being investigated. This also means the reported magnetic hysteresis parameters are not those of the specimen alone but those of the specimen-inspection head magnetic circuit. Work is underway on developing a computer algorithm that can characterize the iron C-core and remove its influence on the flux density measurement, giving the true magnetic parameters of the specimen. This algorithm is not complete at the time of writing.

A magnetic hysteresis measurement typically consists of the following steps:

- 1) Demagnetizing the region of interest
- 2) Magnetizing through one hysteresis cycle
- 3) Calculating magnetic hysteresis parameters

A demagnetization cycle consists of cycling the field while continuously decreasing the amplitude to zero. This leaves the material effectively demagnetized and provides a reference magnetic state which can always be returned to.

The magnetization through one hysteresis cycle involves magnetizing in one direction to a previously determined amplitude, reversing the field to an equal but negative amplitude then reversing again to the positive amplitude.

The calculation of the magnetic hysteresis parameters is performed immediately after the conclusion of a hysteresis cycle by the data analysis software. The approximately 900 data points on the B,H plane can be smoothed, if necessary, through a three-point least squares fit technique.

CHAPTER 3. LABORATORY SCALE STRESS DETECTION WITH A SOLENOID

Introduction

This chapter deals with monitoring the magnetic parameters in materials while applying a tensile stress in the elastic range. The purpose was to determine the magnitude of change in the parameters from solenoid measurements and eventually compare this with changes in parameters from inspection head measurements.

Materials and Experimental Procedure

The materials for this test were two tensile test bars of cylindrical cross section, each 46 cm (18 in.) in length. One bar was made of AISI 4130 and had a diameter of 1.27 cm (0.5 in.). The other bar was made of AISI 4140 and had a 0.64 cm (0.25 in.) diameter. The heat treatment history of the bars was not known. Loading was entirely in the tensile regime and performed by a Tinius Olsen Electromatic Universal Testing Machine. The specimens were loaded in steps up to approximately 70% of yield strength.

Magnetic field measurements were made by a tangential Hall plate on the surface of the specimen. The probe was positioned to measure the field in the axial direction. The magnetic flux was measured by a flux coil of 100 turns of AWG

23 wire on the specimen. The magnetic field was generated by a solenoid which enclosed the specimen. The solenoid was powered by and the resultant field measured by the lab based hysteresisgraph unit. All measurements were taken while the specimen was under desired load. The acquired B,H curves of 944 points were smoothed 3 times using a 5-point smoothing routine. The magnetic hysteresis parameters were then plotted vs. applied stress.

Results and Discussion

Figures 3.1 and 3.2 show the hysteresis loops of the samples at zero and maximum stress. In both cases the loop acquired in the stressed state was narrower and steeper on the sides. The sample of 4130 had a decreased maximum induction at its maximum stress of 405 MPa (59 ksi). This decrease in the induction came after an increase at smaller stresses. This effect was attributed to the Villari reversal. The maximum induction in the 4140 decreased as stress was increased beyond 300 MPa (44 ksi, see Figure 3.7) but not as much as the 4130. The diminished Villari effect may be due to the increased carbon content of the 4140.

The change in the hysteresis parameters versus stress are presented in Figures 3.3 through 3.7. The first parameter, hysteresis loss is shown versus applied stress for both materials (Figure 3.3). There was a decrease of 4709 ergs/cc

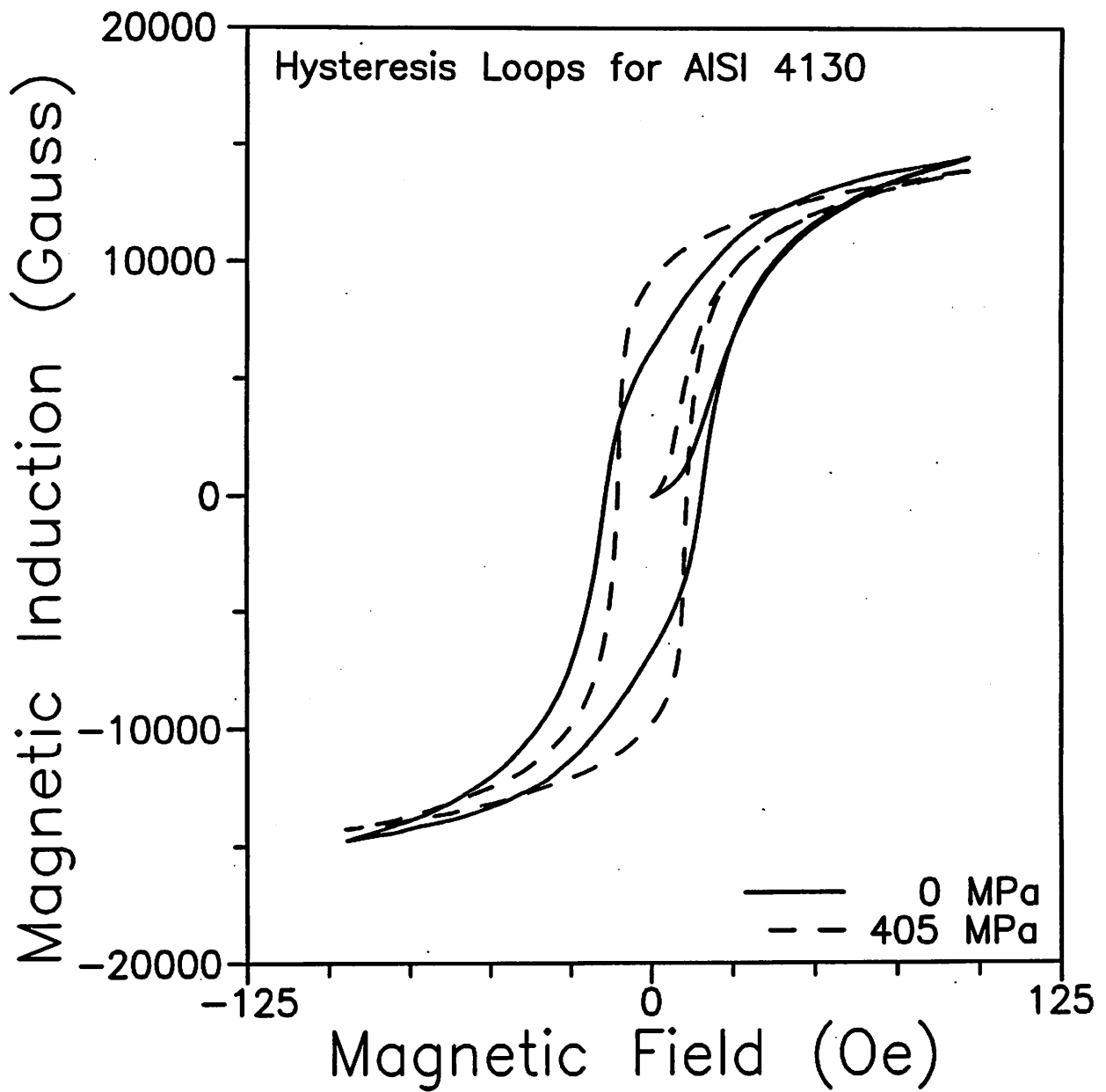


Figure 3.1: Hysteresis loop of AISI 4130 at 0 and 405 MPa

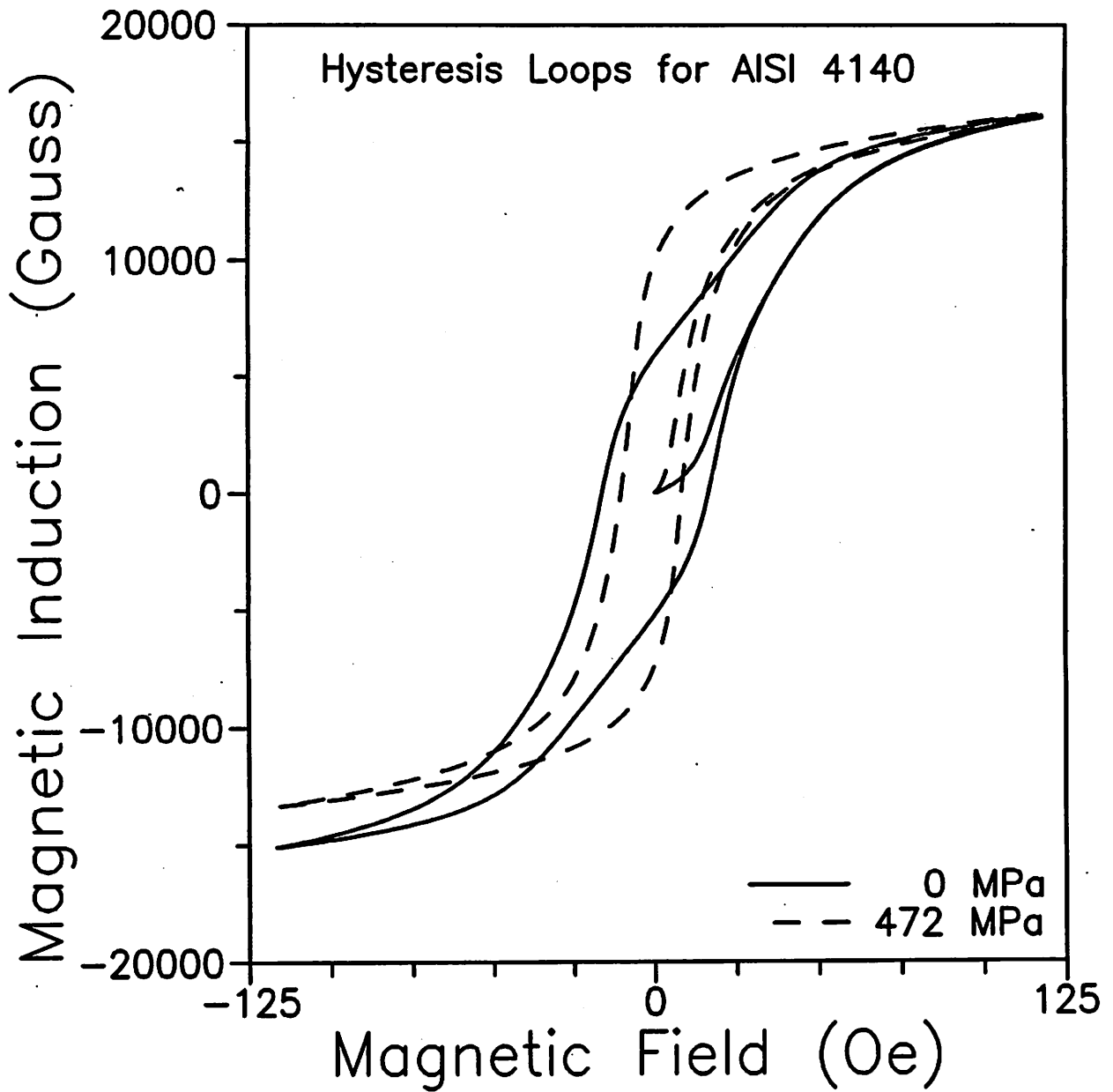


Figure 3.2: Hysteresis loop of AISI 4140 at 0 and 472 MPa

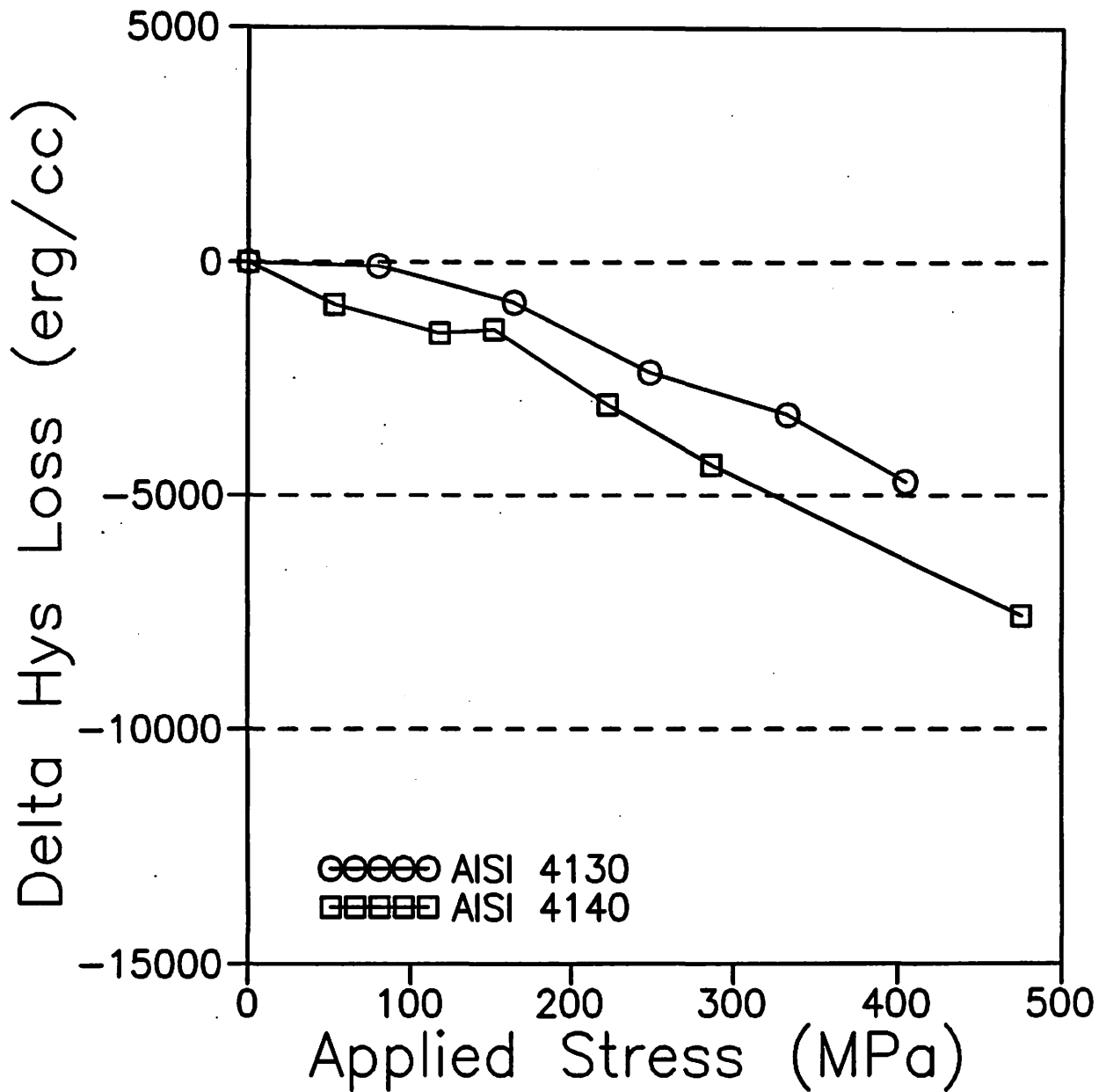


Figure 3.3: Change in hysteresis loss (from zero stress value) for samples of 4130 and 4140

(9.3%) in the 4130 and 7561 ergs/cc (13.8%) in the 4140 as the tensile stress was increased. There was no abrupt change in the slope as the yield point was exceeded. The approximate slope of the curves ($dH_c/d\epsilon$) was -11.6 erg/cc-MPa for the 4130 and -15.9 erg/cc-MPa for the 4140. The change in coercivity with stress is shown in Figure 3.4. There was a decrease of 4.09 Oe (27.7%) in the 4130 and 7.17 Oe (43.9%) in the 4140. The decrease was monotonic up to the yield stress. The rate of decrease changed when the material yielded (at about 300 MPa) after which it changed only slightly. The decline in the hysteresis loss and coercivity up to the yield point was expected. The magnetic anisotropy energy of the domains was reduced in the tensile direction making it easier to move domain walls. Since domain wall motion is represented by the steep portion of the hysteresis loop, this region would be reduced, thus reducing the overall hysteresis loss. The change in the rate of decline in the coercivity was probably due to networks of dislocations that began forming near the yield point. The dislocations would have inhibited domain wall movement, causing an increase in the coercivity.

Changes in the remanence due to the stress can be seen in Figure 3.5. The remanence increased for both materials up to around 300 MPa, after which it decreased, probably due to the Villari reversal. The remanence of the 4130 sample increased 3368 Gauss (52.5%) from zero stress to 333 MPa (48 ksi). In the 4140, the remanence increased by 4607 Gauss (83.3%) from

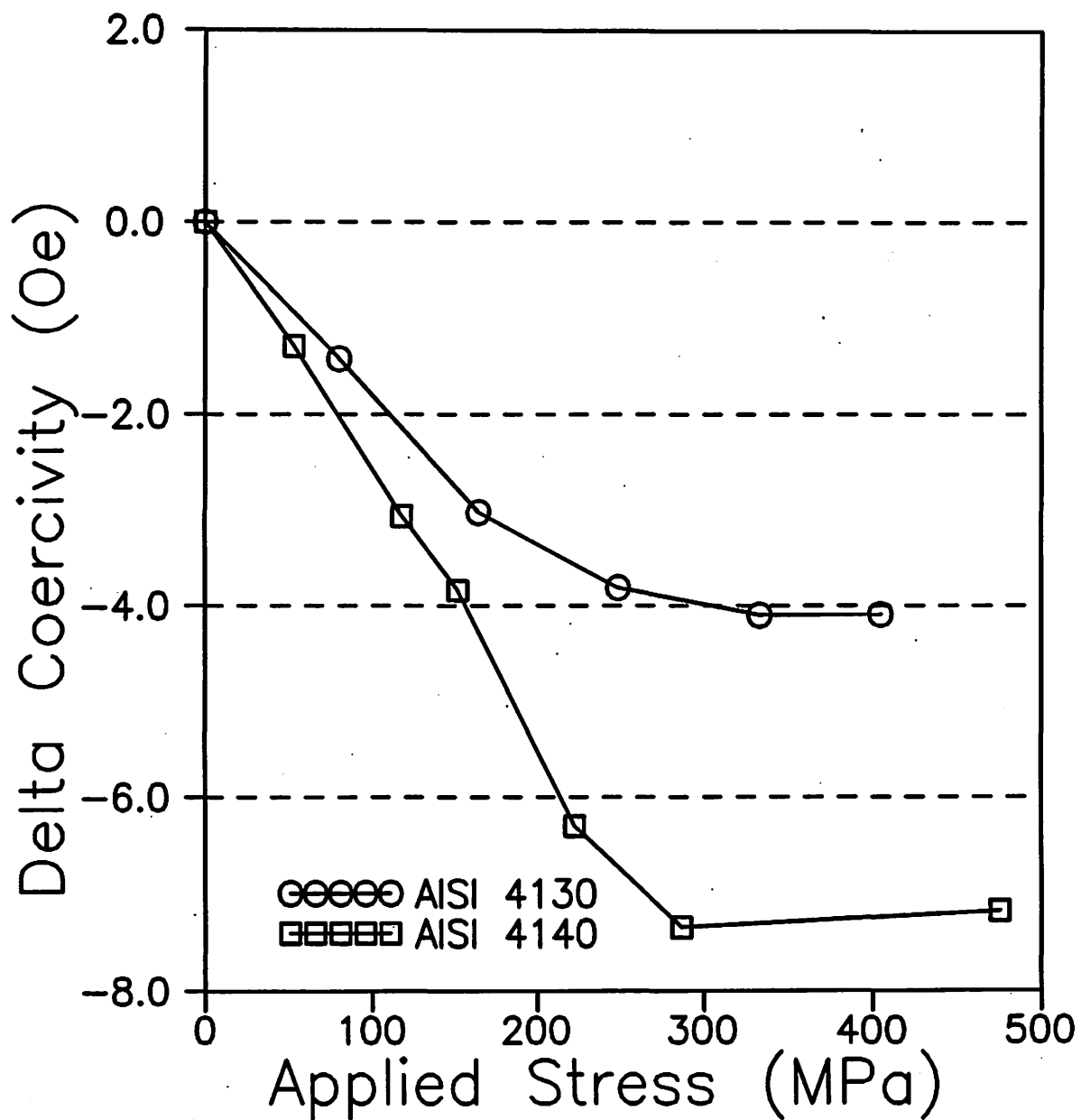


Figure 3.4: Change in coercivity (from zero stress value) for samples of 4130 and 4140

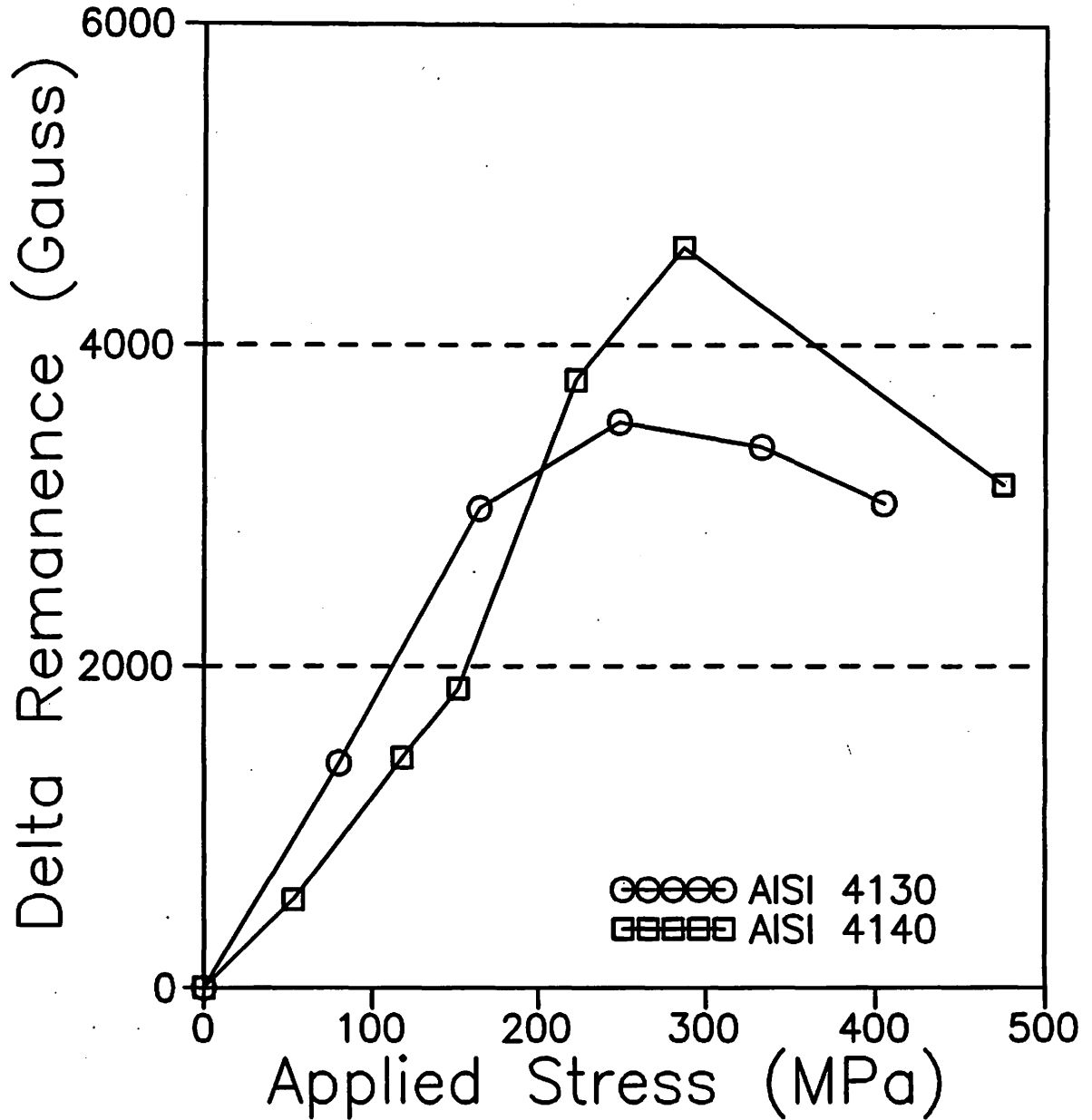


Figure 3.5: Change in remanence (from zero stress value) for samples of 4130 and 4140

zero to 287 MPa (42 ksi). A similar variation is seen in the plot of the changes in the maximum differential permeability, Figure 3.6. The sample of 4130 showed an increase of 2617 (292%) before reversing trend. The sample of 4140 showed an increase of 516 (84.0%) before reversing. The increases in the remanence and maximum differential permeability were due to the reduction in the anisotropy energy from the tension. These two parameters are very strongly dependent on the anisotropy energy, as evidenced by the large relative changes observed. The lower anisotropy energy along the direction of tensile stress ensures that it is easier for the domains to align along this direction and therefore the permeability would be greater.

The maximum induction versus applied stress is shown in Figure 3.7. The sample of 4130 experienced a slight increase in induction at low stresses but then decreased as the stress was increased. The sample of 4140 had an increase in the maximum induction until it reached the Villari reversal point, after which it experienced a slight decline. The sample of 4130 decreased 2.4% until it reached yield stress and the 4140 increased 5.0% until the Villari reversal point was reached.

Conclusions

There are definite trends in the hysteresis parameters as tensile stress is increased along the direction of the applied

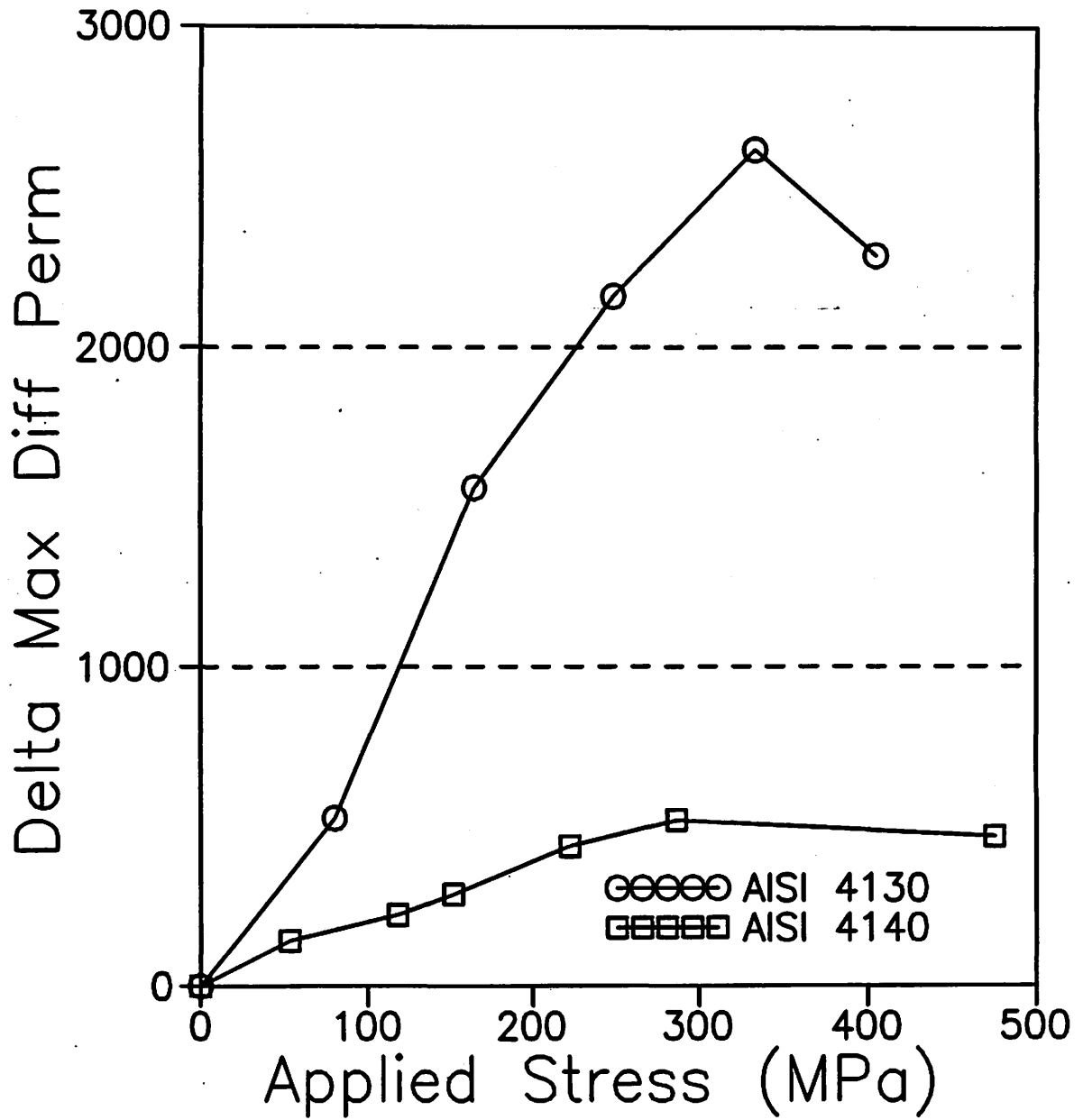


Figure 3.6: Change in maximum differential permeability (from zero stress value) for samples of 4130 and 4140

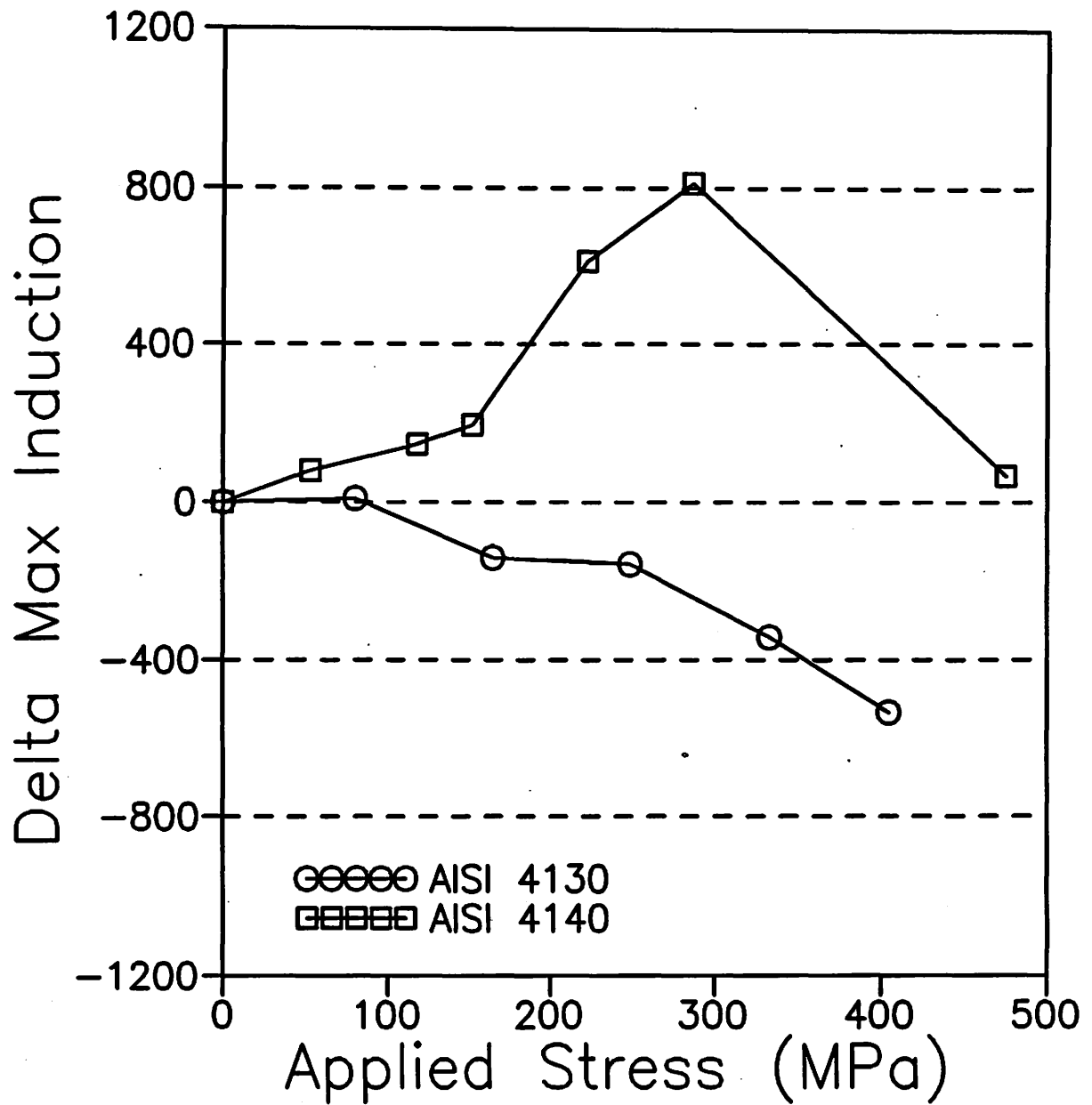


Figure 3.7: Change in maximum induction (from zero stress value) for samples of 4130 and 4140

magnetic field. The hysteresis loss and coercivity have been seen to decrease with tensile stress in the elastic range. The remanence and maximum differential permeability have been seen to increase with increasing tensile stress up to the Villari reversal point, this can be explained on the basis of existing theory. These changes with stress were attributed to the stress contribution to the magnetic anisotropy energy due to the stress. After yielding though, the trends seen in the parameters reverse. This was attributed to the production of dislocations from the plastic deformation, which effectively pin magnetic domain walls and so lead to changes in coercivity and hysteresis loss.

CHAPTER 4. APPLIED STRESS MEASUREMENT USING INSPECTION HEAD

Introduction

This chapter deals with monitoring the magnetic parameters in various rail materials while applying various elastic stresses. The magnetic measurements were performed by an inspection head on the surface of the specimens. The goal was to see if changes in the magnetic parameters due to stress can be monitored without a solenoid and without wrapping a flux coil around the specimen.

Materials and Experimental Procedure

The materials for this test were 9 flat tensile specimens of rail steel representing different metallurgies and heat treatments. Each specimen was machined from the web of a rail with known metallurgy. None of the railroad rail had been in service, they came direct from the steel mills and so represent a variety of compositions and heat treatments in their original, "as received" state. The composition of each specimen is given in table 4.1. A brief description of the origin of each rail is given in table 4.2. Optical micrographs were made from each tensile specimen and are given in Figures 4.1 through 4.9. A discussion of the microstructure will be given in the next section.

Table 4.1: Chemical composition of laboratory rail specimens

Element	W1	W2	W3	W4	W5
Carbon	0.79	0.73	0.76	0.74	0.80
Manganese	1.15	0.97	1.03	1.04	0.71
Phosphorous	0.013	0.017	0.012	0.014	0.025
Sulfur	0.012	0.023	0.039	0.013	0.023
Silicon	0.69	0.25	0.25	0.23	0.29
Nickel	0.02	0.09	0.05	<0.01	<0.01
Chromium	0.91	0.11	0.12	0.21	0.61
Molybdenum	0.02	0.02	0.02	<0.01	0.21
Copper	0.02	0.22	0.21	0.01	0.02
Vanadium	0.097	----	----	----	----

	W6	W15	W23	CF&I
Carbon	0.78	0.80	0.75	0.79
Manganese	1.03	1.01	0.67	0.98
Phosphorous	0.019	0.029	0.026	0.019
Sulfur	0.035	0.032	0.021	0.019
Silicon	0.20	0.30	0.33	0.32
Nickel	0.06	0.04	0.06	0.09
Chromium	0.12	0.24	0.64	0.22
Molybdenum	0.02	0.01	0.18	0.02
Copper	0.29	0.04	0.08	0.35
Vanadium	----	----	----	----

Table 4.2: Identification of railroad web sections studied

Identification	Description
W1	Krupp Cr-V
W2	Bethlehem Fully Heat Treated
W3	Bethlehem Medium Hardness
W4	Wheel-Pitt Inter. Hardness
W5	Wheel-Pitt Cr-Mo
W6	Bethlehem Standard Carbon
W15	Sacilor Stretch Straightened
W23	Wheel-Pitt Cr-Mo (same as W5)
CF&I	CF&I

The rectangular tensile specimens were 46 cm (18 in.) long and the cross sectional area in the gage region was 4.5 cm² (0.7in²). The specimens were machined smooth, so there was no scale coating on any of the specimens by the time the measurements were made.

Magnetic hysteresis measurements were made by mechanically clamping the inspection head onto the specimen in the center of the gage region. The inspection head was positioned so that the flux path was parallel to the stress axis. The inspection head remained clamped to the specimen throughout loading, and measurements were made while the material was held at load. Measurements were taken at 5 different stress levels, applied in the following order: 0, +100, -100, +200, -200 MPa (0, +14.5, -14.5, +29, -29 ksi).

The magnetic hysteresis parameters were recorded after smoothing the 944 data points on the hysteresis curve 3 times using a 5-point smoothing routine. The magnetic parameters were then plotted versus applied stress.

Results and Discussion

Figures 4.1 through 4.9 are optical micrographs of the different specimens at 200x. All exhibit a pearlitic microstructure consistent with a eutectic composition. Although quantitative studies were not performed, it is evident from W2 and W15 that grain size varied from ASTM grain



Figure 4.1: Photomicrograph of sample W1, showing pearlitic microstructure. Nital etch, originally 200x

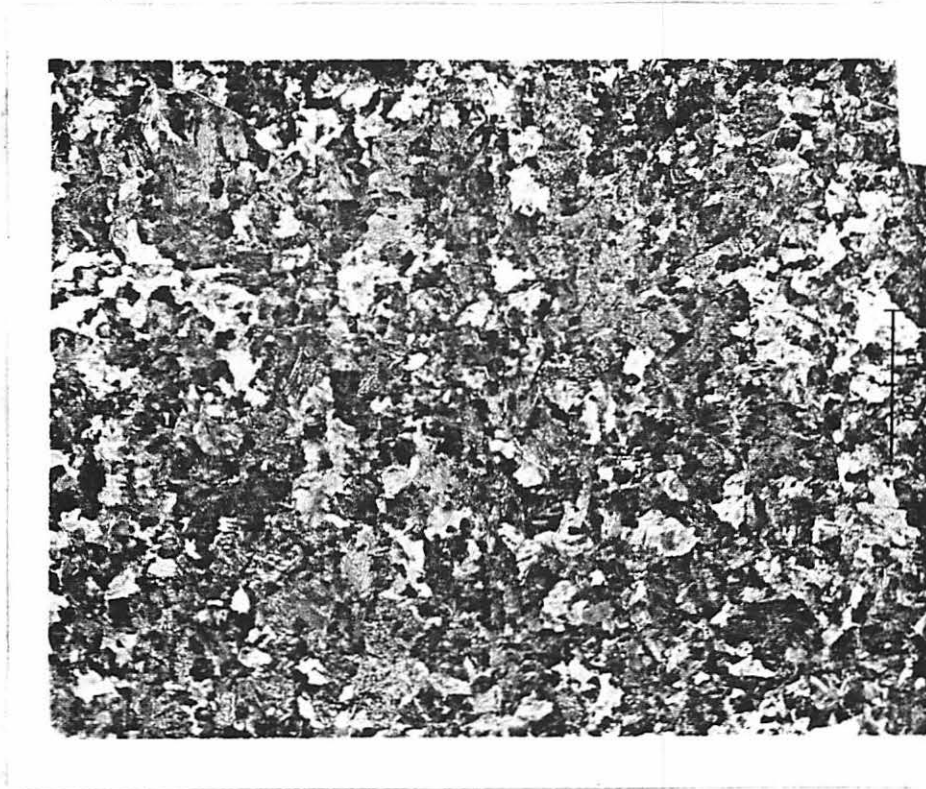


Figure 4.2: Photomicrograph of sample W2, showing pearlitic microstructure. Nital etch, originally 200x

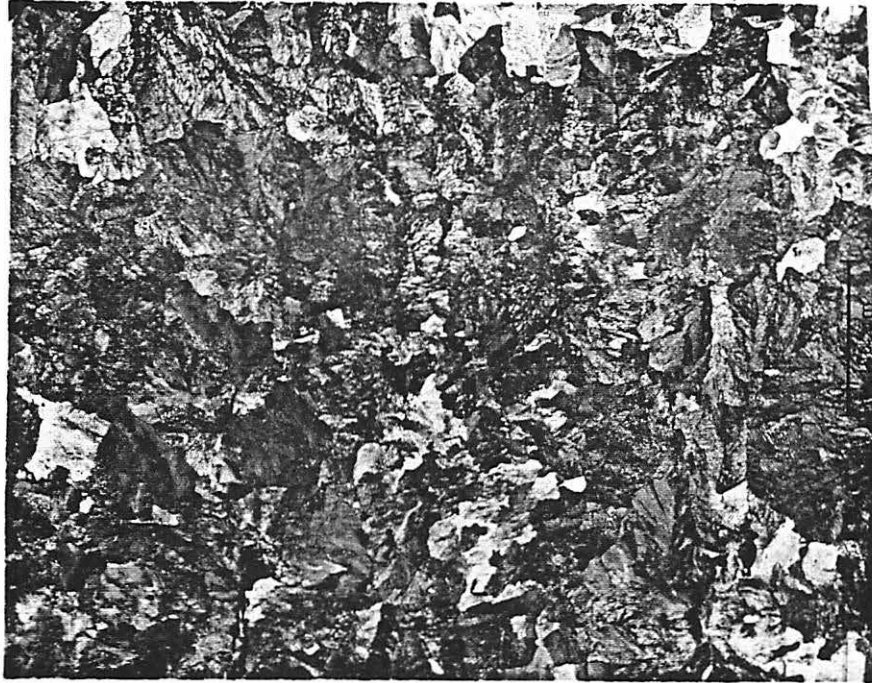


Figure 4.3: Photomicrograph of sample W3, showing pearlitic microstructure. Nital etch, originally 200x



Figure 4.4: Photomicrograph of sample W4, showing pearlitic microstructure. Nital etch, originally 200x



Figure 4.5: Photomicrograph of sample W5, showing pearlitic microstructure. Nital etch, originally 200x



Figure 4.6: Photomicrograph of sample W6, showing pearlitic microstructure. Nital etch, originally 200x



Figure 4.7: Photomicrograph of sample W15, showing pearlitic microstructure. Nital etch, originally 200x



Figure 4.8: Photomicrograph of sample W23, showing pearlitic microstructure. Nital etch, originally 200x



Figure 4.9: Photomicrograph of sample CF&I, showing pearlitic microstructure. Nital etch, originally 200x

size 3 to 6. Samples W2, W3 and CF&I had the smallest pearlitic colonies. No single reason for the variation in grain sizes can be found due to the large number of composition differences although sample W2 probably had a small grain size due to heat treating effects. It was the only rail in the group studied which had been fully heat treated, oil quenched and tempered. The rest of the rails were induction heated in the head region and air cooled. The oil quench of rail W2 would produce the smaller grains. Samples W5 and W23 were very similar to each other both in microstructure and composition.

Figure 4.10 is a plot of the hysteresis loops from sample W15 at three stress states, -200, 0 and +200 MPa (-29, 0, and +29 ksi). The loop measured at -200 MPa was not as steep on the sides as the loop measured at zero stress. The loop measured at +200 MPa was steeper on the sides than the zero stress loop. This effect is similar to that observed in the previous chapter, where stress was found to alter the hysteresis curves of samples measured in a solenoid. The fact that similar effects can be seen in components via a surface measurement without first having to place them in a solenoid is encouraging because it points to the possibility of using the magnetic hysteresis technique as a stress evaluation tool. Changes in the hysteresis loop were most likely due to alteration of the magnetic anisotropy energy in the field direction due to the stress. This agrees with the Jiles-

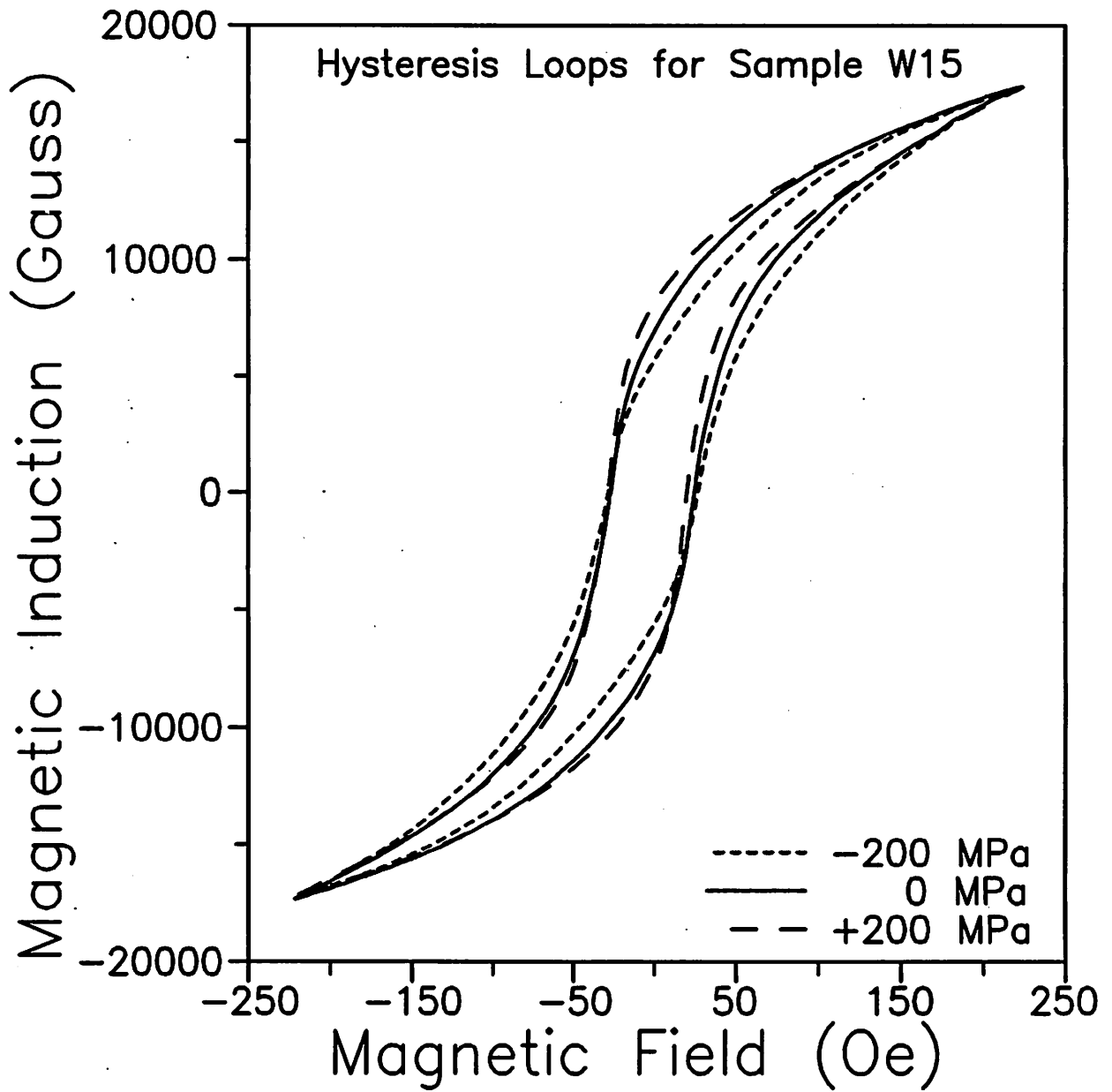


Figure 4.10: Hysteresis loops for sample W15 at different stress levels

Atherton theory of hysteresis (27).

Contrary to the results reported in the previous chapter and those of Kwun and Burkhardt (12), there was little change in the maximum induction at the higher stresses. This is perhaps due to the fact that the stress levels here were somewhat smaller than in the previous measurements and also that there is a different magnetization flux path, consisting of a tensile specimen (undergoing stress) and an inspection head (not undergoing stress). In this case the maximum induction depended on the magnetization characteristics of two components, one of which was not being stressed.

Figure 4.11 is a difference plot showing the change in remanence versus applied stress for the specimens. In all the specimens the remanence decreased as compressive stress was increased. The average drop in remanence from zero stress to -200 MPa (-29 ksi) was over 13.6%. With the exception of W1, the remanence of the specimens increased with increased tension. The increase from zero stress to +200 MPa (+29 ksi) averaged 4.2%, and was therefore less than the change due to compression. The increased sensitivity to compressive stresses is not understood at the present time.

The role of microstructure on the magnetic properties can be seen here. At zero applied stress, the remanence varied from 6591 to 8126 Gauss. The mechanically harder materials such as the Cr-Mo alloys (W5, W23) had a larger remanence than softer material such as the Bethlehem standard carbon rail

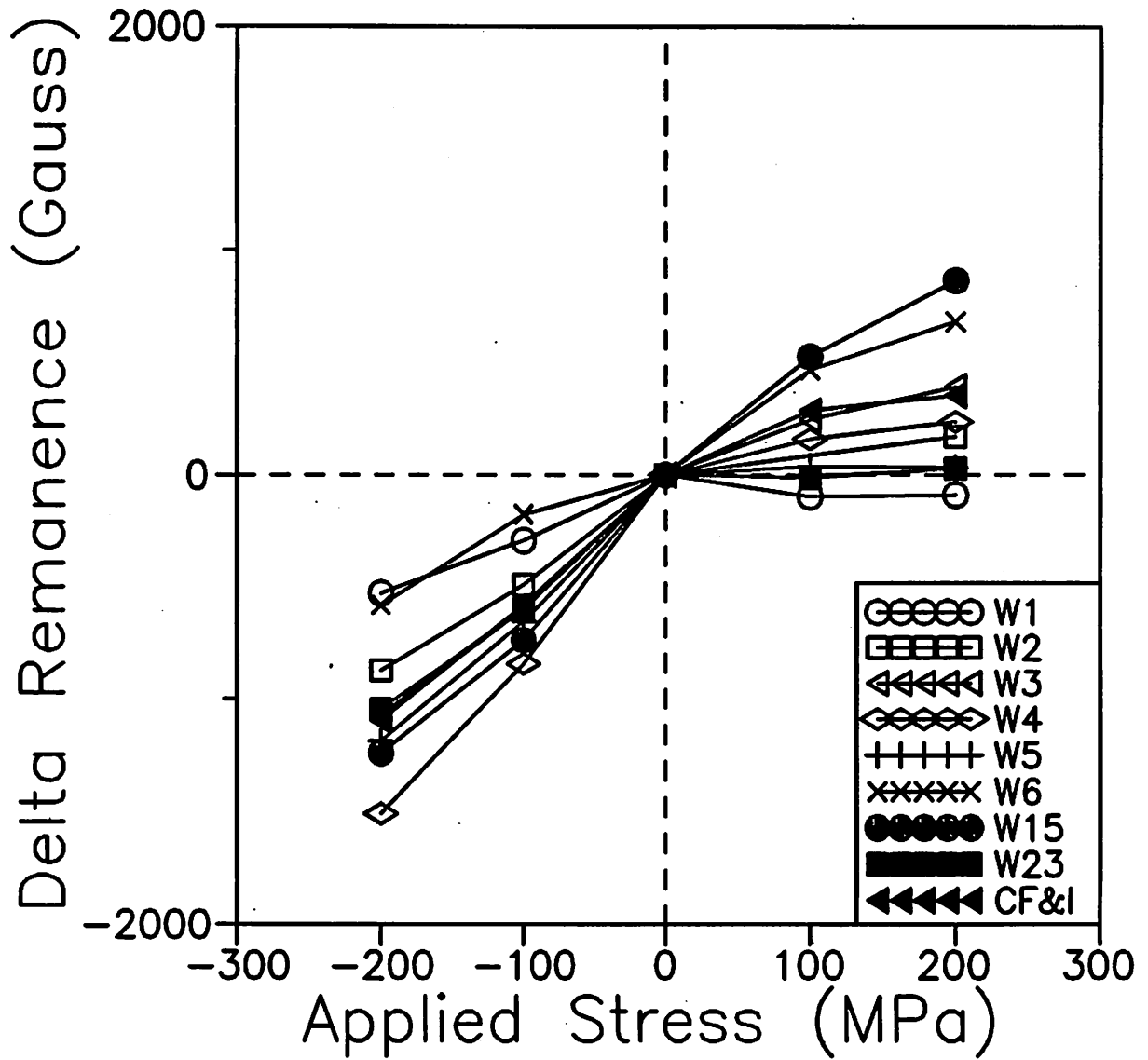


Figure 4.11: Change in remanence [$(B_r)_{\sigma=0} = 0$] with stress

(W6). The Cr-V alloy (W1), a relatively hard material, was the only sample which showed a reduction in remanence, and was also the only sample to contain vanadium. The addition of vanadium tends to substantially reduce the magnetic induction of the material through solid solution hardening.

Figure 4.12 shows the maximum differential permeability as a function of stress. There is a similar pattern here as seen for remanence. There are very sharp decreases in the permeability with increasing compression. Some of the materials, such as CF&I, W15 and W6 showed increases in permeability in response to tensile stresses. Some others showed minimal increase (W3, W4, W5 and W23), while in two of the specimens, W1 and W2, the permeability actually decreased in response to increasing tension. The samples that showed increases in permeability with tension were all quite similar in composition so it was expected that they would behave similarly. The samples that underwent a decrease in permeability with increasing tension (W1, W2) were also comparable except that W1 has a higher Si and Cr content. These two behaved similarly but were displaced on the graph.

Figure 4.13 is a plot of the coercivity versus stress. As can be seen, there were only slight changes in response to stress. All the samples showed a slight decrease in response to increasing tension, and a slight increase with increasing compression. The coercivity is not widely regarded as a strong indicator of elastic applied stress. It is most

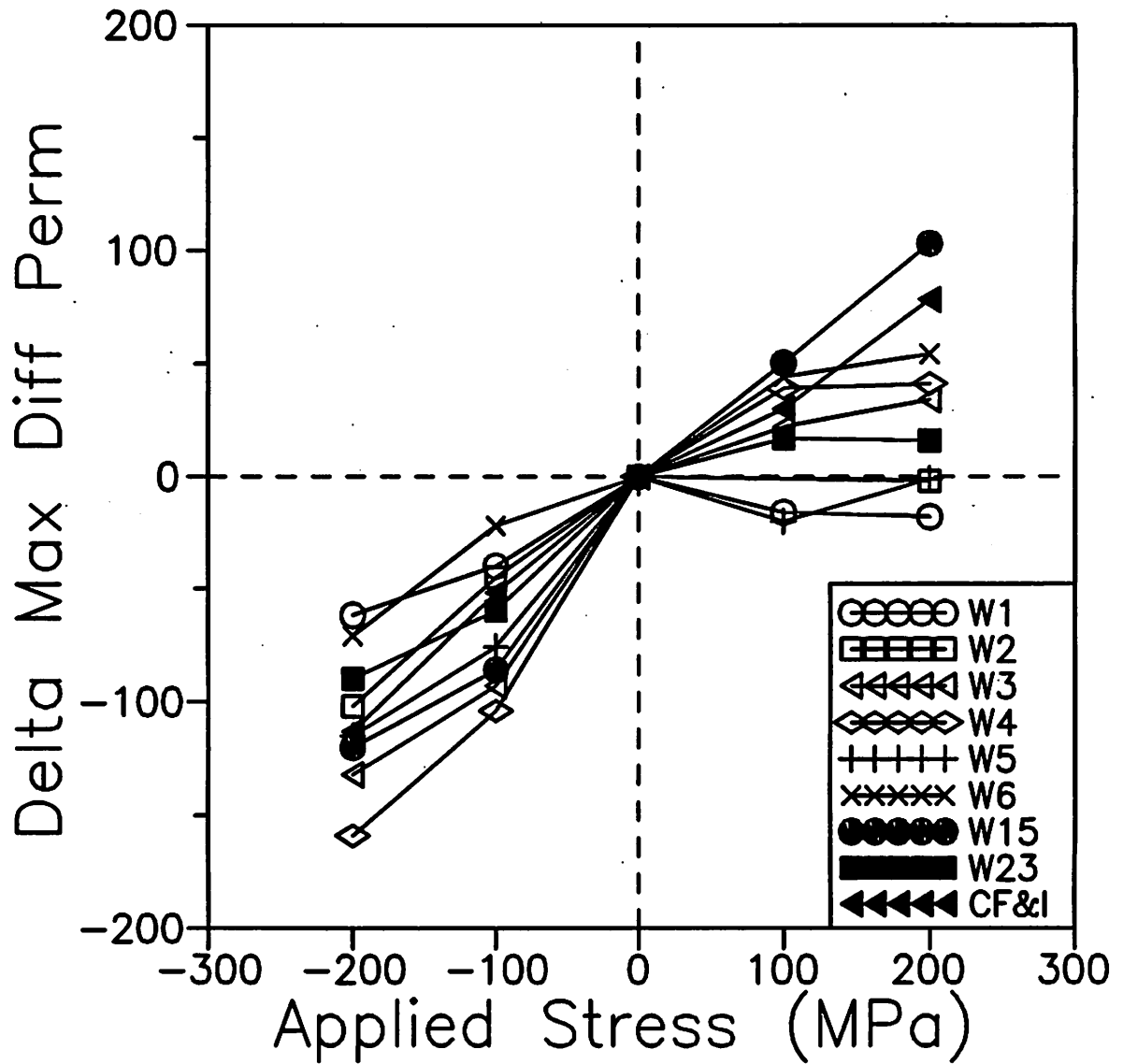


Figure 4.12: Change in maximum differential permeability [$(\mu'_{\max})_{\sigma=0} = 0$] with stress

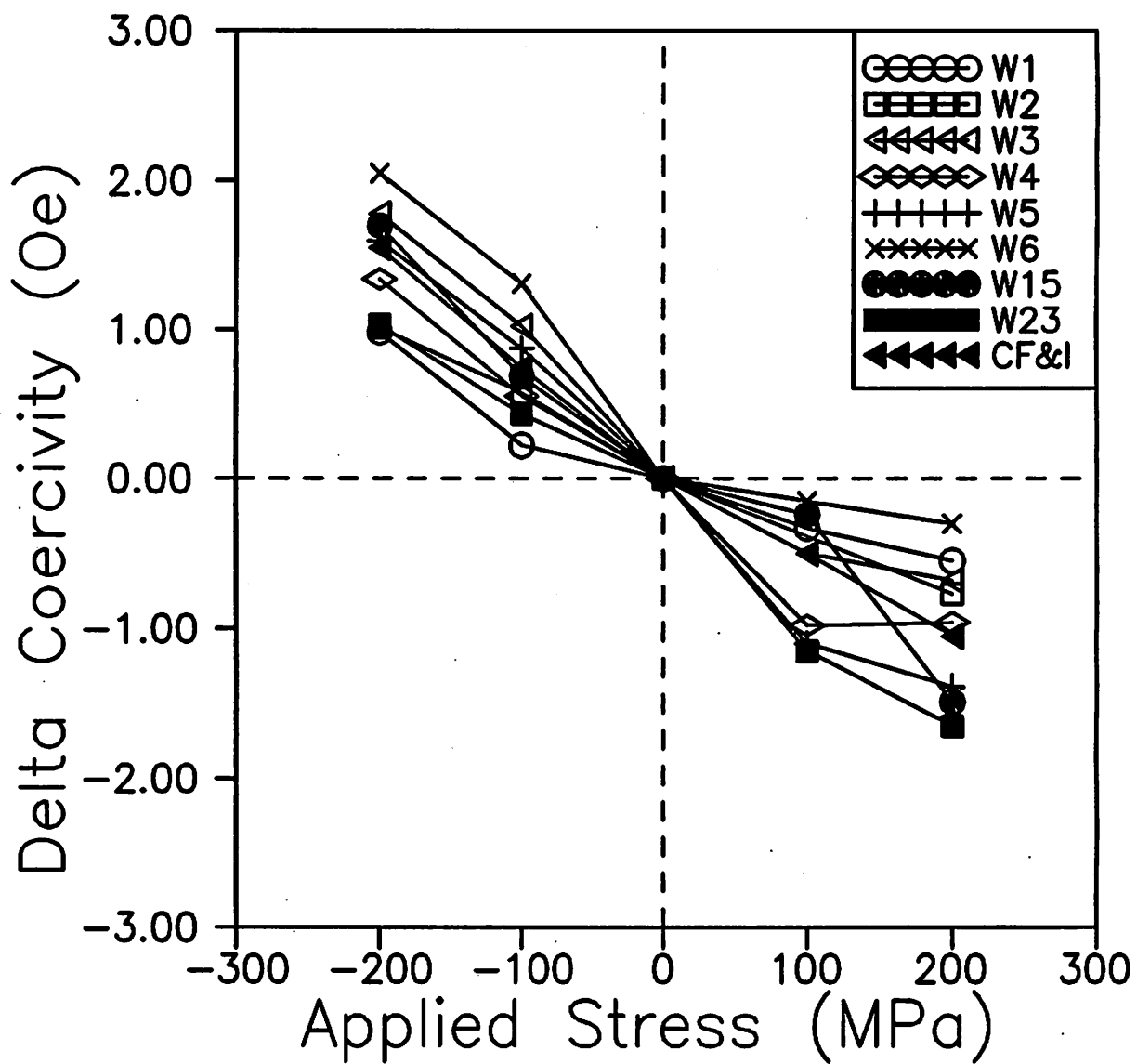


Figure 4.13: Change in coercivity [$(H_c)_{\sigma=0} = 0$] with stress

influenced by microstructure and composition. At zero applied stress the coercivity varied from 40.2 Oe (sample W1) to 19.7 Oe (sample W6). The chromium content seems to play a significant role. Higher chromium content led to larger coercivity. This is probably due to precipitation of chromium carbides (Cr_{23}C_7) that help strengthen the material.

Conclusions

The change in the hysteresis parameters with stress in various laboratory specimens were successfully monitored by using an inspection head placed on the surface of the specimens. Increasing tension increased the remanence and the maximum differential permeability while it decreased the hysteresis loss and coercivity. Increasing compression generally decreased the remanence and maximum differential permeability while it increased the hysteresis loss and coercivity. The microstructure of the specimens played a role in determining the rate of change in the magnetic parameters with stress.

CHAPTER 5. COMPARISON BETWEEN LABORATORY AND RAIL COMPONENTS

Introduction

The previous chapter discussed applied stress measurements in laboratory test specimens using a surface magnetic measurement. For the magnetic hysteresis technique to become a viable NDE tool, its effectiveness at detecting applied stress in railroad rail must be proven. Before moving to stress detection in railroad rail, correlations between the laboratory test specimens and railroad rail specimens must be made. The goal of this chapter was to find the differences in magnetic properties between the lab specimens and rail specimens due to the scale coating and the curvature of the rail.

Materials and Experimental Procedure

For this section, a number of lab test specimens studied in the previous chapter were compared against the original rail from which they were made. The rails were approximately 46 cm (18 in.) long and had a scale coating. None of the rails had experienced service conditions.

Measurements on the rail specimens were made with the inspection head located in the center of the web region with the pole pieces aligned parallel to the length of the rail.

Measurements on the corresponding lab test specimens were made by placing the inspection head in the center of the specimens in the unstressed condition. The hysteresis loss, coercivity, remanence and maximum differential permeability were plotted for the laboratory test and rail specimens.

Results and Discussion

Figures 5.1 and 5.2 are plots of the hysteresis loss and coercivity respectively, measured for both groups of specimens. The parameters varied for each specimen within a group but the relative positions for each metallurgy between groups remained about the same. The difference in readings between the two groups is due to two factors, the presence of a scale coating on the rail, and the curvature of the web region on the rail.

The scale coating influences the measurement because it acts as a ferrimagnetic region between the poles of the inspection head and the rail metal. In effect, it raises the inspection head up off the rail metal. This is similar to a lift off effect. With the poles of the inspection head slightly above the metal, there is a major disturbance in the magnetic flux path and thus the magnetic hysteresis parameters will be expected to change.

The curvature of the web region produces a similar lift off effect on the inspection head because there is no longer

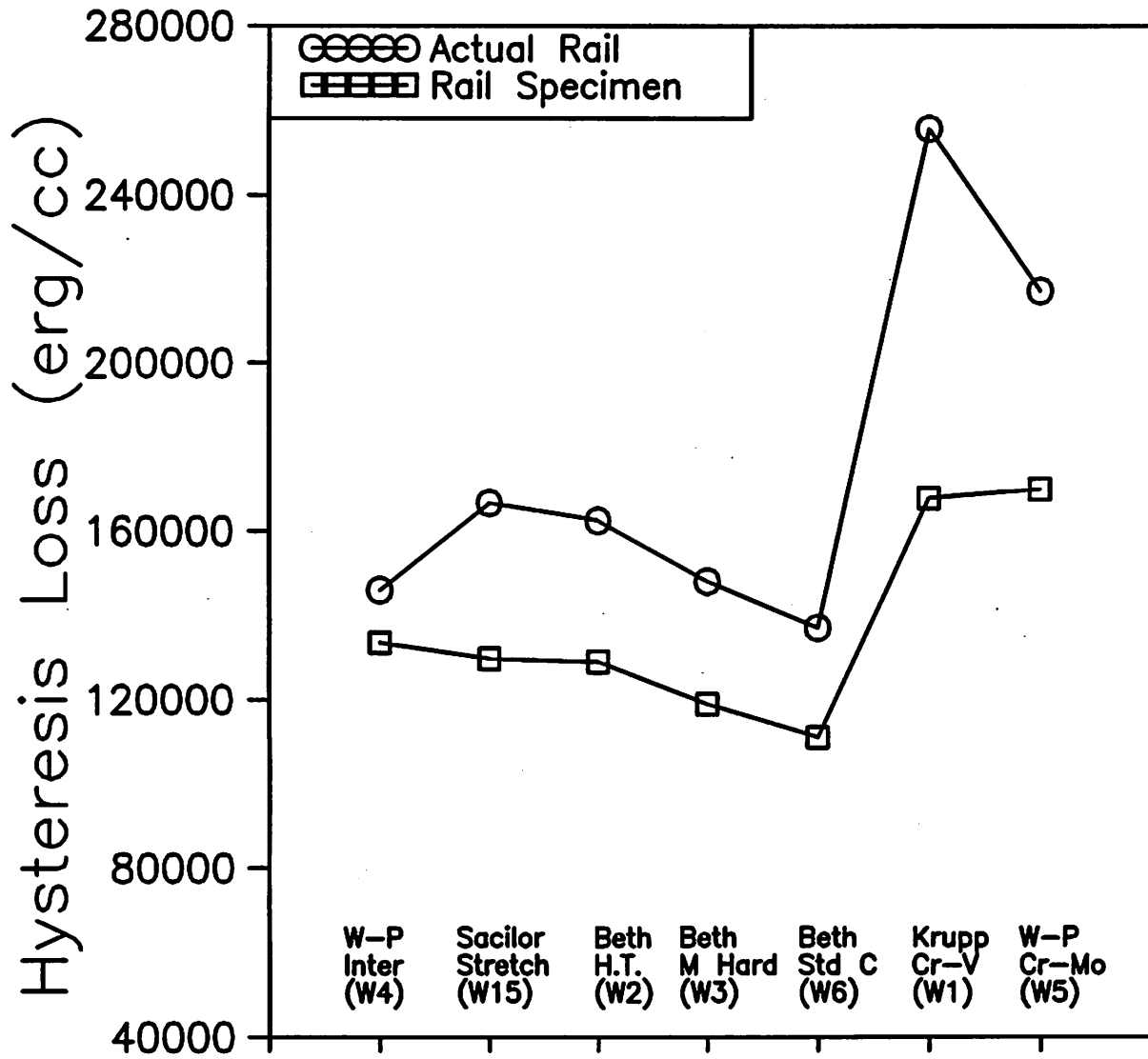


Figure 5.1: Hysteresis loss measured on various laboratory and rail specimens

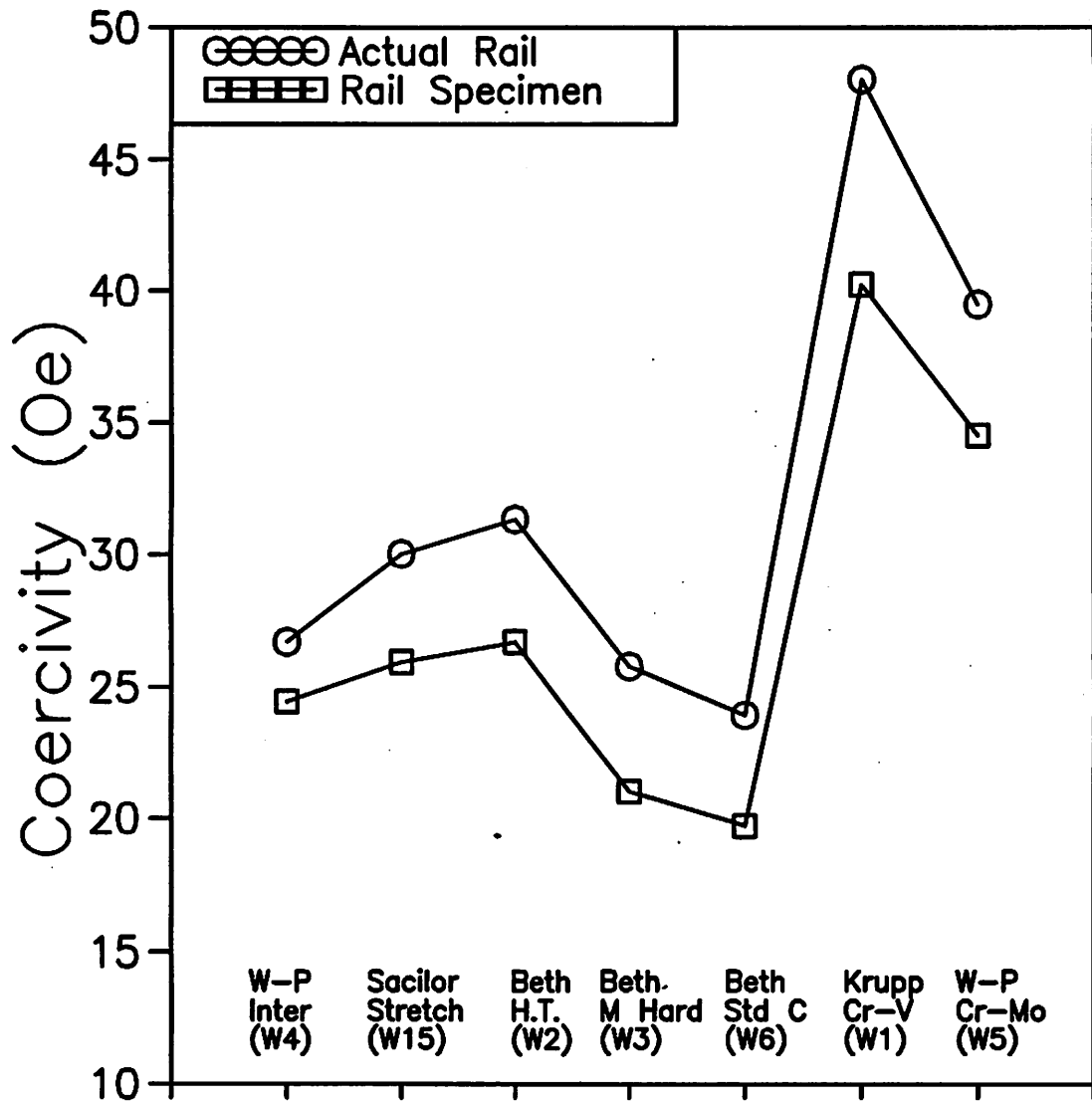


Figure 5.2: Coercivity measured on various laboratory and rail specimens

100% contact between the inspection head and the rail. The fact that the relative positions of the parameters between groups stays the same is encouraging because it seems that some information about a material can be gained even through external interferences.

Figures 5.3 and 5.4 show the remanence (fig. 5.3) and maximum differential permeability (fig. 5.4) measured on the specimens. No information can be gained from these parameters.

Conclusions

Microstructure played a major role in determining the magnetic response of a ferromagnetic material. Surface conditions, such as scale and curvature also affected the inspection head measurements because of changes in the flux path. However the essential variation of magnetic properties with stress for example has been found to be superimposed on those changes.

After comparing a group of laboratory rail specimens with sections of railroad rail of corresponding microstructures, it was found that the relative values of the hysteresis loss and coercivity remained constant. This shows that the transfer from laboratory measurements to field measurements can be achieved by the use of appropriate magnetic inspection equipment such as the Magnescope.

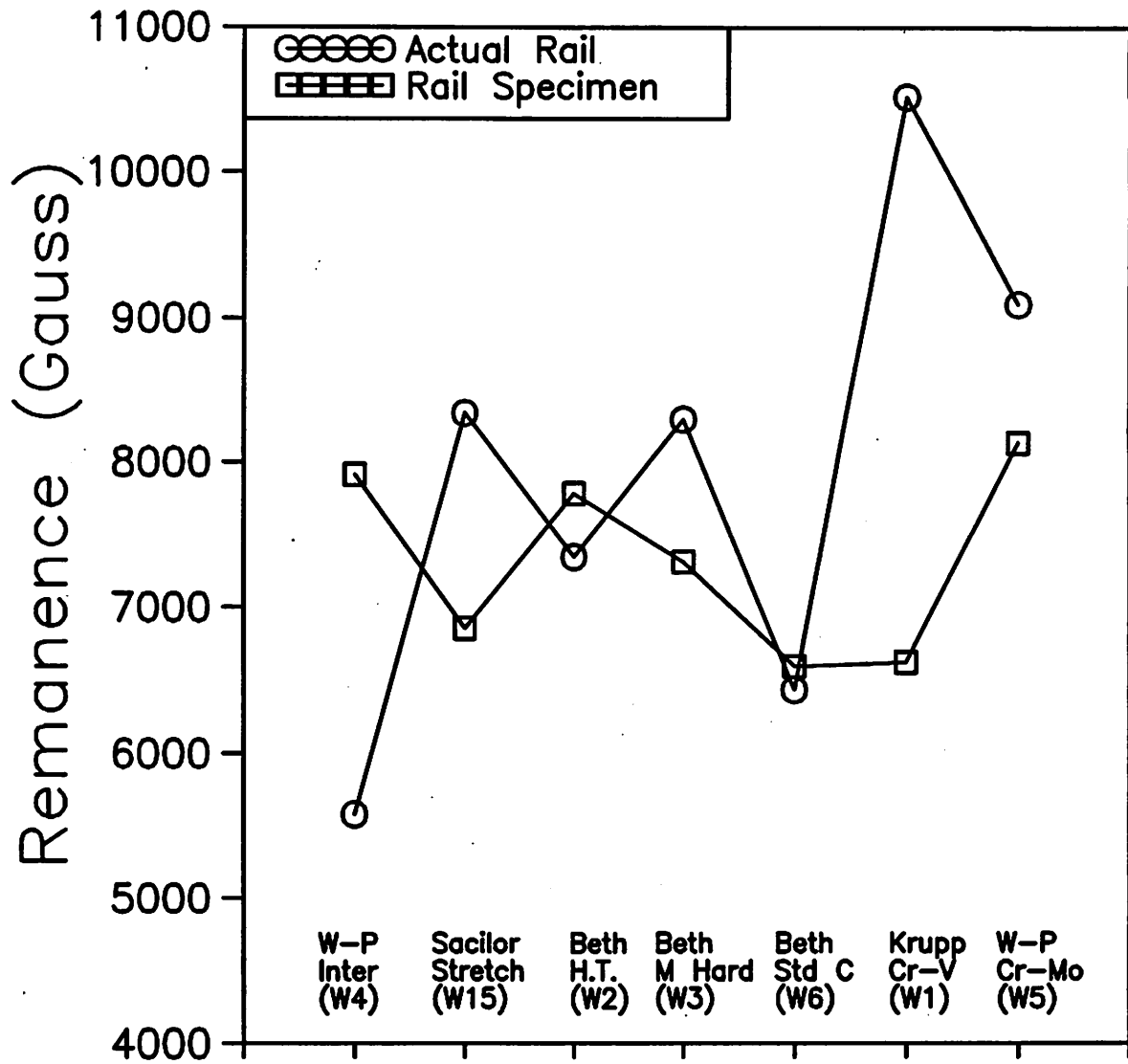


Figure 5.3: Remanence measured on various laboratory and rail specimens

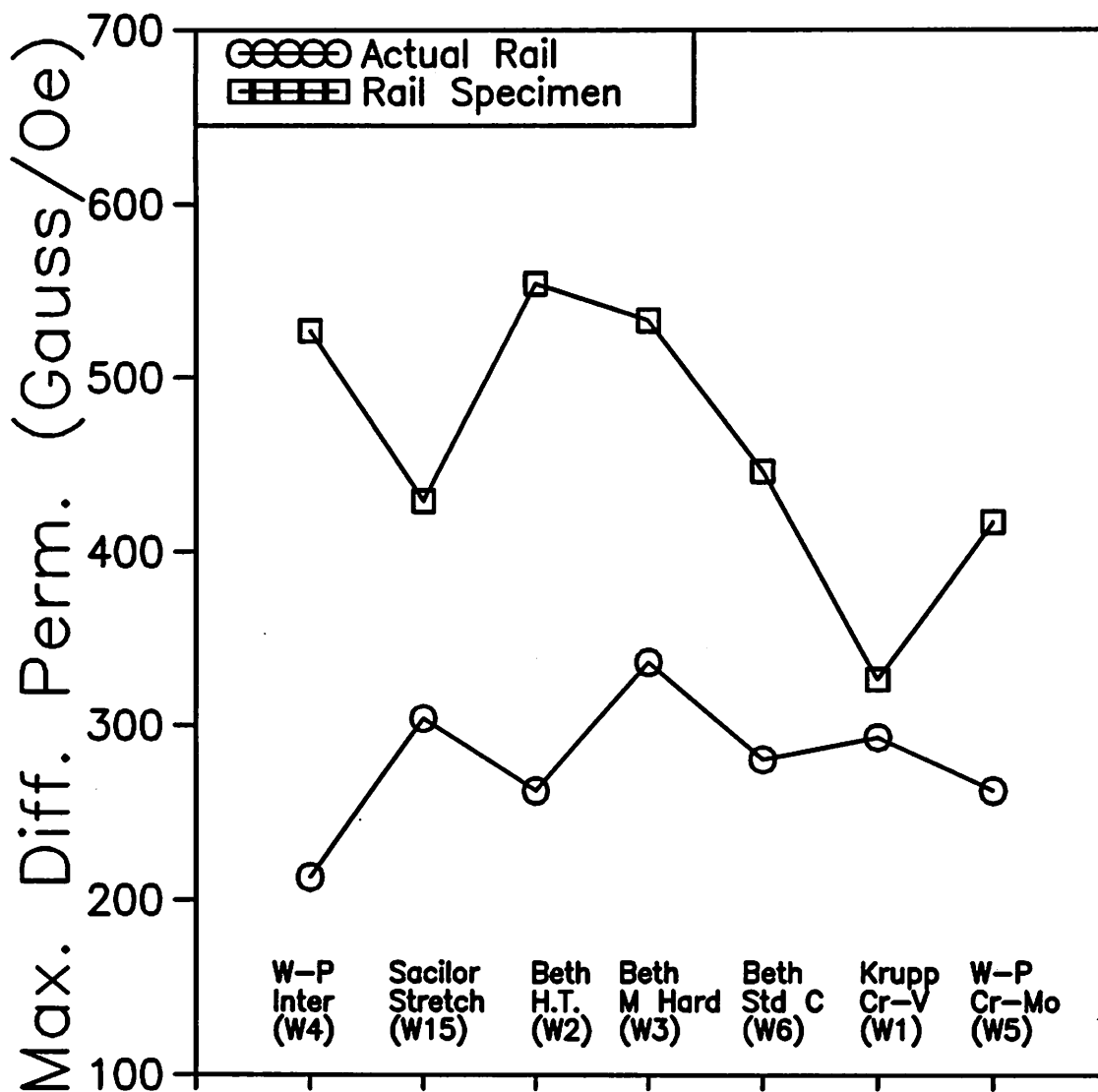


Figure 5.4: Maximum differential permeability measured on various laboratory and rail specimens

CHAPTER 6. APPLIED STRESS MEASUREMENTS IN RAILROAD RAIL

Introduction

The previous chapter compared the magnetic characteristics of unstressed laboratory test specimens and corresponding railroad rail sections. Differences in the parameters were noted but these were attributed to the dissimilar surfaces between the groups. It was judged that the bulk magnetic properties could still be detected. This chapter deals with continuing those rail section measurements to stress detection.

Materials and Experimental Procedure

A two meter length of standard carbon railroad rail was placed in a rail puller for applied stress testing. A rail puller is a device which clamps on both ends of the rail in the web region. The clamps were connected to hydraulic cylinders which, depending on their position and orientation, can apply and sustain either a compressive or tensile load on the length of the rail. Strain gages attached to the web of the rail near the center showed the maximum strain to be about ± 330 microstrains. This works out to a maximum stress of approximately ± 70 MPa ($\pm 10,000$ psi). The rail puller was used to apply a controlled and sustained elastic stress on the

rail in two steps, half maximum (about 165 microstrains) and full maximum strain (about 330 microstrains). The rail was strained to half maximum, full maximum then released. This constituted one stress (strain) cycle. Three stress cycles in the tensile direction and three stress cycles in the compressive direction were performed.

The inspection head was attached by a C-clamp to the web of the rail. The inspection head was placed in the center of the length of rail near the strain gage location. The poles of the inspection head were aligned so that the flux path was along the rolling and stress direction.

The magnetic measurements were made after achieving the desired elastic stress; ie. zero, half maximum or full maximum. The inspection head was kept in place while the strain was changed, although it needed to be removed for changing the set up of the rail puller from tensile to compressive testing.

Results and Discussion

Figure 6.1 is a plot of a hysteresis loop measured at zero stress on the web of the rail. The levelling of the curve at the loop tips indicated that the material was probably near saturation. All subsequent measurements achieved the same level of saturation.

Figure 6.2 shows the change in maximum differential

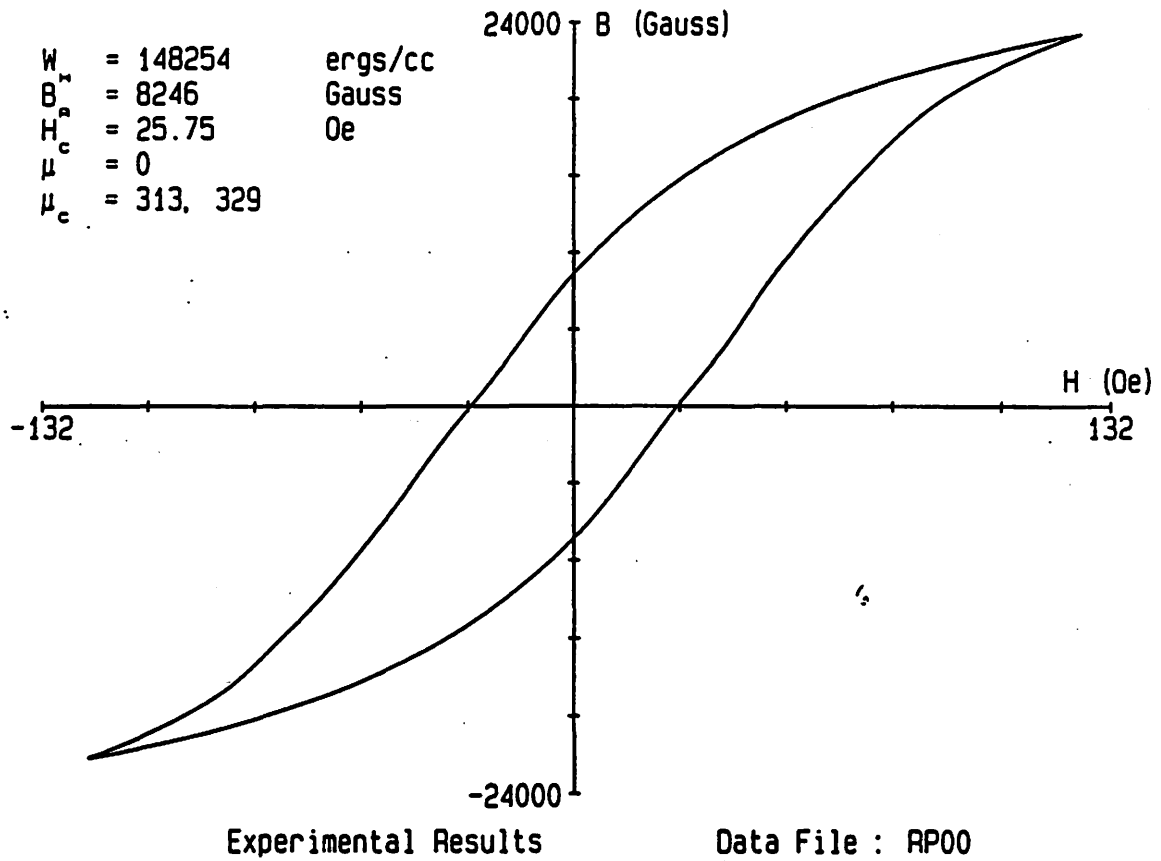


Figure 6.1: Hysteresis loop measured on web of rail at zero stress

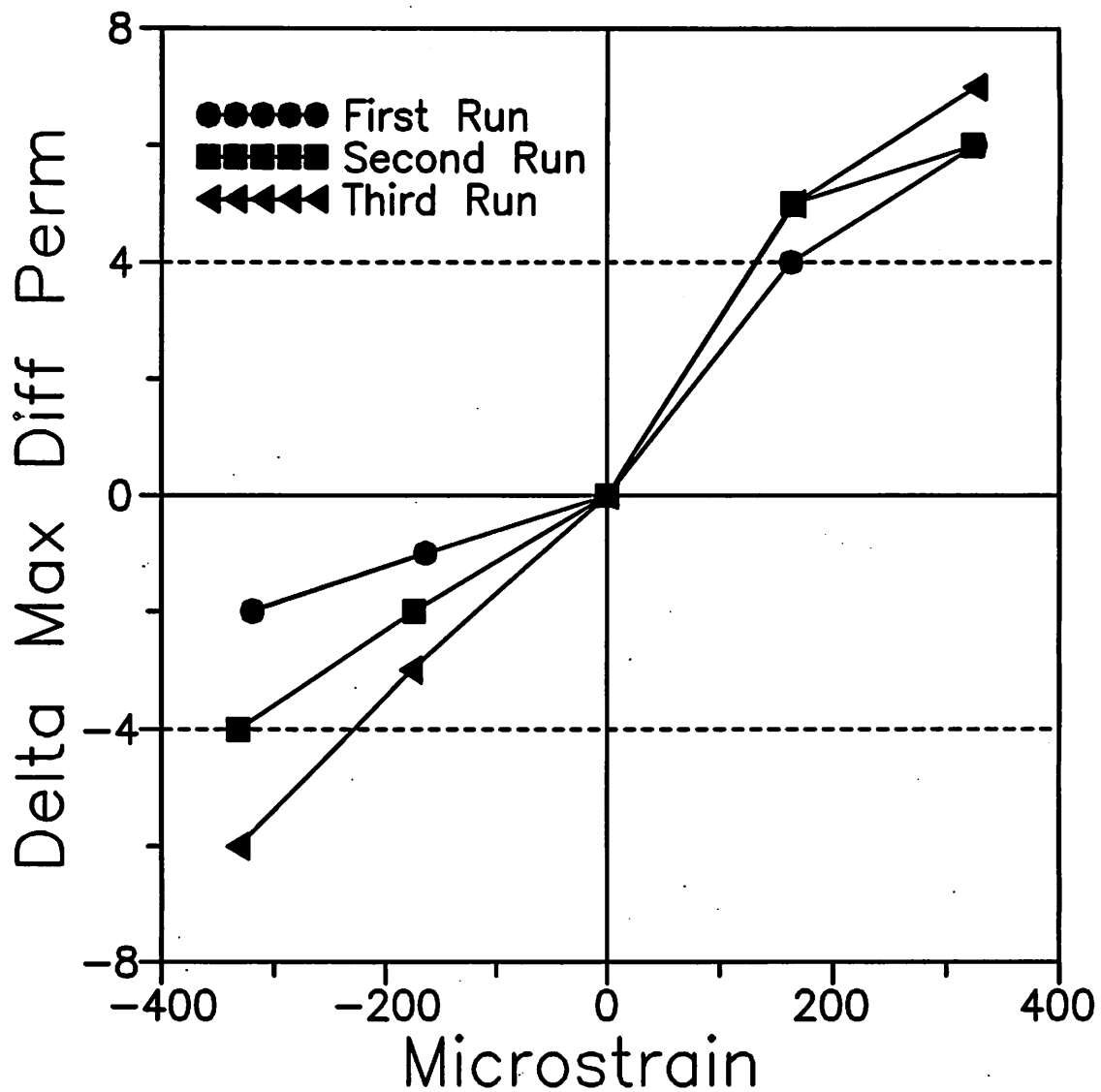


Figure 6.2: Change in maximum differential permeability $[(\mu'_{\max})_{\epsilon=0} = 0]$ with strain

permeability from zero strain for three tension cycles and three compression cycles. The three tension cycles increased the permeability as the stress was increased. The three compression cycles decreased the permeability as the stress was increased. The change, $d\mu/d\sigma$ was larger in the tensile regime. The average slope in the tensile direction was 0.019 μ /strain while in the compressive direction it was 0.012 μ /strain. Every tensile cycle produced a change in the permeability of about 7 G/Oe, while the maximum change in the permeability due to compression ranged from 2 to 6 G/Oe. These are admittedly small changes but it should be noted that these measurements were made on a curved surface (the inspection head pole pieces are flat) that was coated with rust and scale. These are far from ideal laboratory conditions but it is these conditions that will be commonly encountered if the magnetic hysteresis technique is to become a viable practical inspection tool.

Table 6.1 shows the actual maximum differential permeability values at the different strain levels. The percent change in the tensile direction averaged 2.0% while in the compressive direction it averaged -1.1%. These changes are similar within experimental error. The average zero stress permeability value for tension and compression mode were radically different. This difference in the zero stress permeability values between the modes was probably due to the different positioning of the inspection head between runs.

Table 6.1: Max. Differential permeability for rail puller runs

<u>Strain level</u>	<u>First Run</u>		<u>Second Run</u>		<u>Third Run</u>	
	Strain ($\times 10^{-6}$)	μ'_{\max}	Strain ($\times 10^{-6}$)	μ'_{\max}	Strain ($\times 10^{-6}$)	μ'_{\max}
<u>Tension</u>						
Zero	0	318	0	318	0	318
Half	163	322	164	323	166	323
Full	325	324	323	324	325	325
<u>Compression</u>						
Zero	0	345	0	349	0	351
Half	-164	344	-174	347	-177	348
Full	-319	343	-332	345	-332	345

The inspection head needed to be removed from the rail while the rail puller was being converted from tension mode to compression mode. Although care was taken to place the inspection head in the same location for the compression cycles as the tension cycles, any slight change would have affected the permeability reading.

The change in remanence with strain is shown in Figure 6.3. The three tension cycles increased the remanence from 75 to 94 Gauss for 325 microstrains. The three compression cycles reduced the remanence by various amounts. The maximum remanence change in compression was a decrease of 56 Gauss for -332 microstrains. The first compression cycle reduced the remanence by only 11 Gauss for -319 microstrains, a far smaller change than either of the other two compression cycles. The reason for this is unknown. The change in

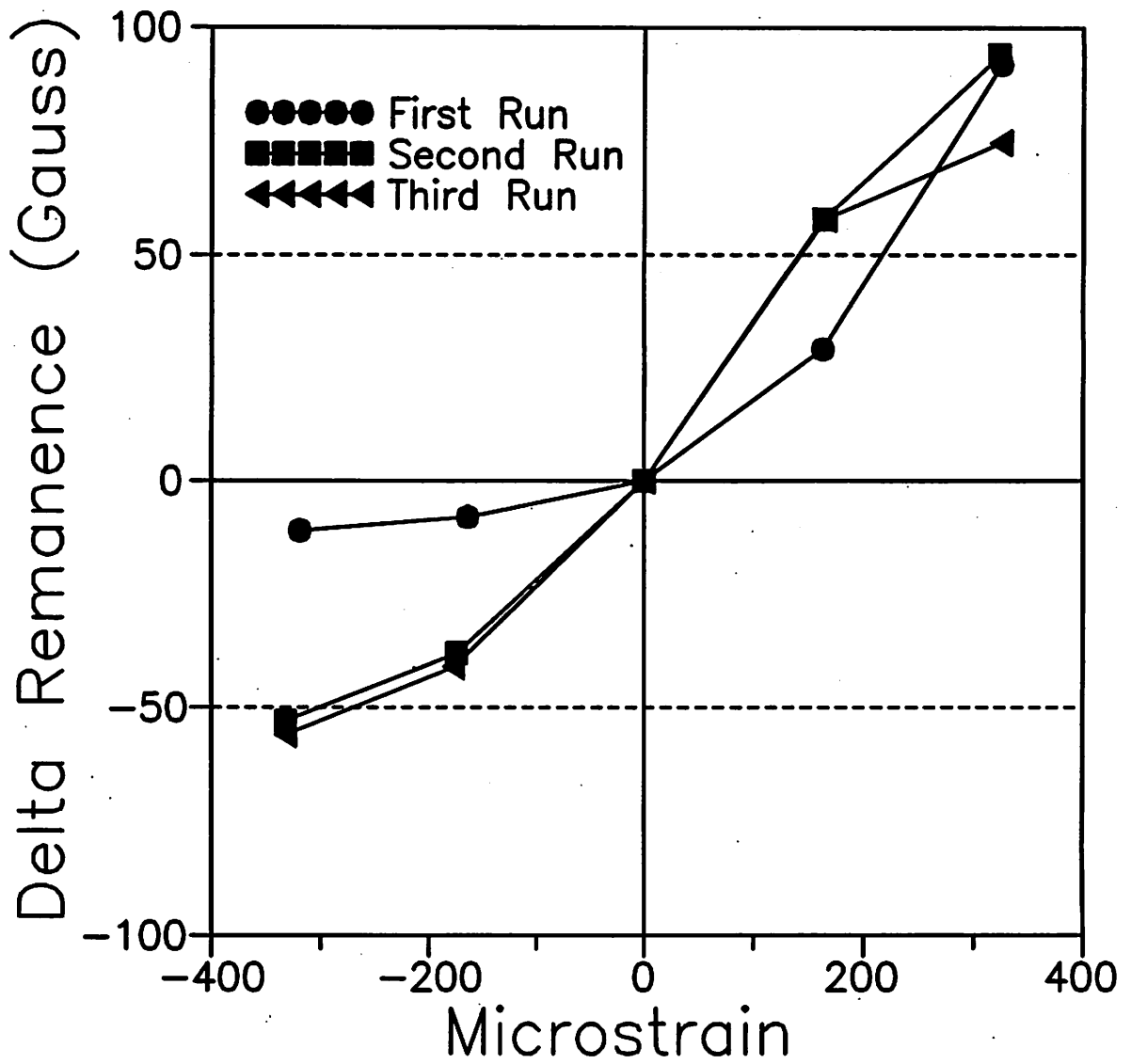


Figure 6.3: Change in remanence [$(B_r)_{\epsilon=0} = 0$] with strain

remanence with elastic strain is larger for tensile strain than for compressive strain. The average slope in the tensile direction was $0.268 \text{ G}/\mu\text{strain}$ while in the compressive direction it was $0.121 \text{ G}/\mu\text{strain}$, indicating a relatively strong sensitivity to stress.

The actual remanence measured for each strain is shown in table 6.2. The percent change in the tensile direction

Table 6.2: Remanence (in Gauss) for rail puller runs

Strain Level	First Run		Second Run		Third Run	
	Strain ($\times 10^{-6}$)	B_r	Strain ($\times 10^{-6}$)	B_r	Strain ($\times 10^{-6}$)	B_r
<u>Tension:</u>						
Zero	0	8256	0	8281	0	8308
Half	163	8285	164	8339	166	8366
Full	325	8348	323	8375	325	8383
<u>Comp.</u>						
Zero	0	8270	0	8318	0	8334
Half	-164	8262	-174	8280	-177	8293
Full	-319	8259	-332	8265	-332	8278

averaged 1.0% while in the compressive direction it averaged 0.5%. The remanence did not return to its zero strain value after completing a stress cycle, regardless of whether it was a tensile or compressive stress. Pitman (18) saw a similar effect but offered no explanation. In (28) Jiles and Atherton

attributed it to the hysteresis curve trying to approach the anhysteretic condition. Figure 6.4 shows the change in hysteresis loss from zero strain for the tensile and compressive cycles. Increasing tension decreased the hysteresis loss while increasing compression tended to increase the hysteresis loss. The changes in hysteresis loss with increasing tension were larger but less consistent. The change in hysteresis loss at maximum tensile strain varied from 3486 to 1875 erg/cc. At maximum compressive strain, the change in hysteresis loss was consistently around +1680 erg/cc. The average slope in the tensile direction was -8.47 erg/cc per μ strain while in the compressive direction it was -5.09 erg/cc per μ strain. These large slopes show that the hysteresis loss could be used as an indicator of stress.

The measured hysteresis loss for each stress cycle is presented in table 6.3. The offset, caused by removing and repositioning the inspection head between tensile and compressive modes was evident. A stress cycling effect is present in both the tensile and compressive regimes. There is a displacement downwards with each stress cycle, similar to an effect seen before by Bozorth (4). The amount of total displacement decreased with each cycle and, according to Bozorth, eventually to zero.

Figure 6.5 shows the change from zero to full strain in the coercivity. As can be seen, increasing tension decreases the coercivity while increasing compression increases the

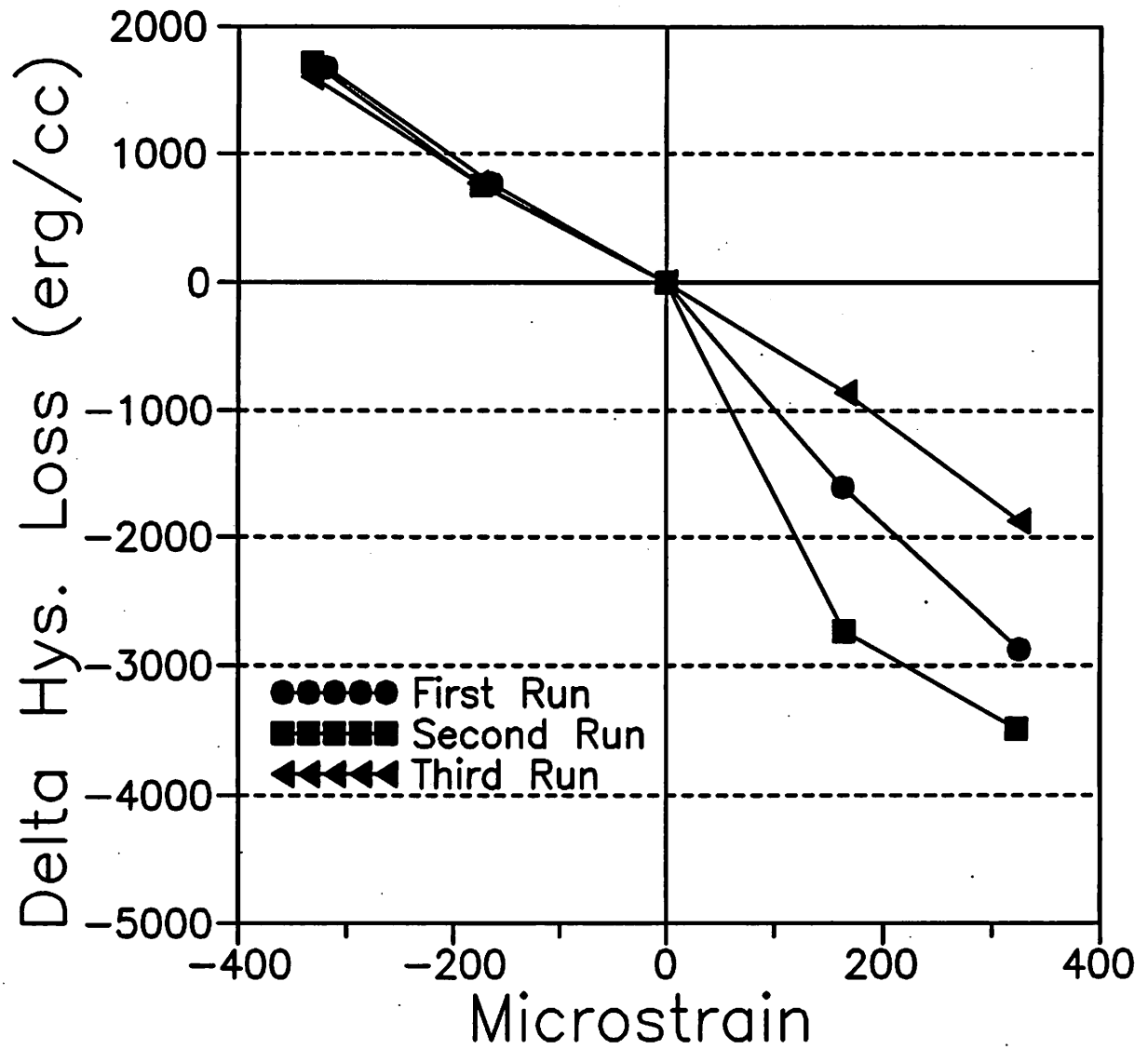


Figure 6.4: Change in hysteresis loss $[(W_h)_{\epsilon=0} = 0]$ with strain

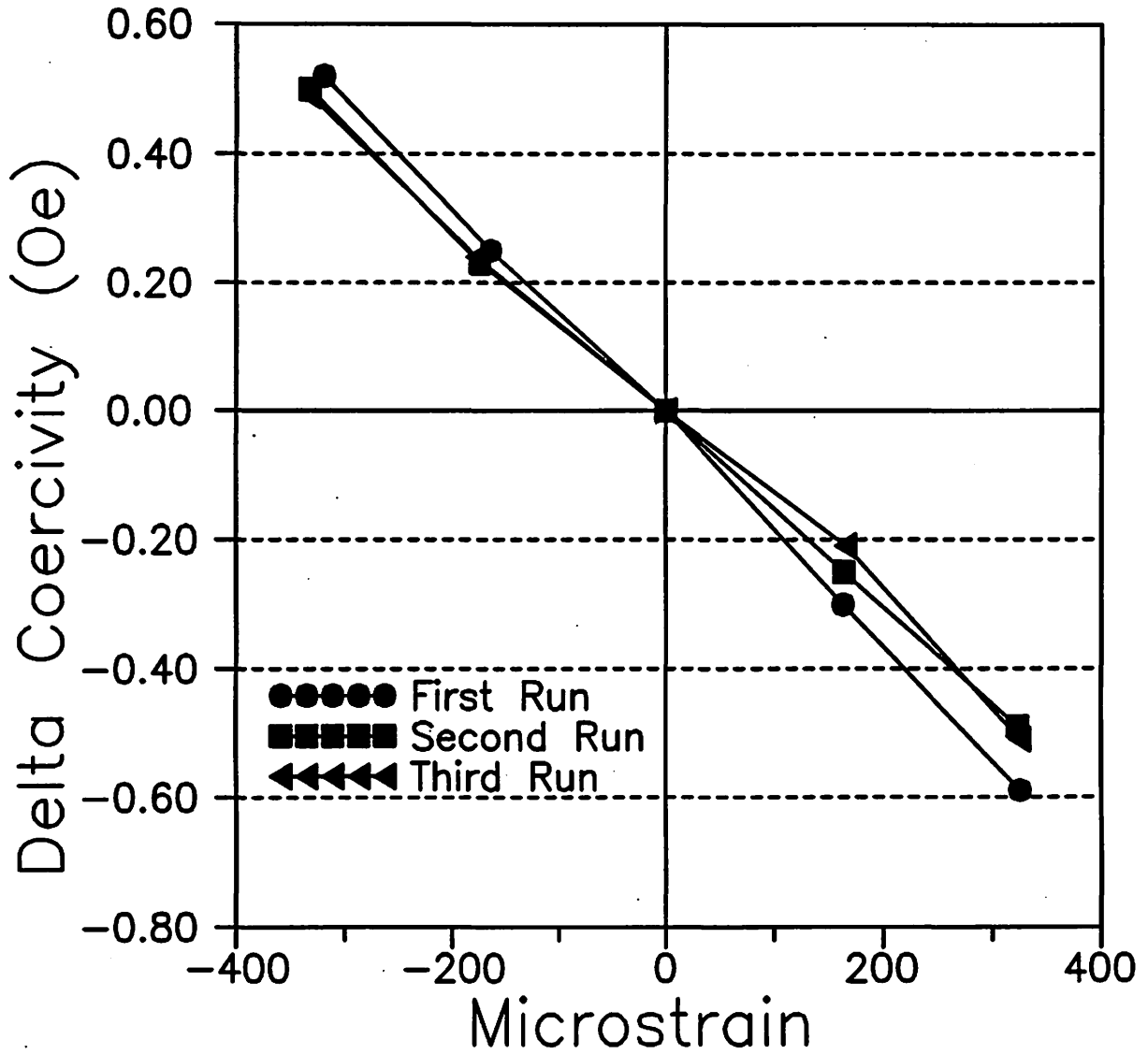


Figure 6.5: Change in coercivity [$(H_c)_{\epsilon=0} = 0$] with strain

Table 6.3: Hysteresis loss (in erg/cc) for rail puller runs

Strain Level	First Run		Second Run		Third Run	
	Strain ($\times 10^{-6}$)	W_h	Strain ($\times 10^{-6}$)	W_h	Strain ($\times 10^{-6}$)	W_h
<u>Tension</u>						
Zero	0	148202	0	147653	0	145452
Half	163	146594	164	144919	166	144597
Full	325	145328	323	144167	325	143577
<u>Comp.</u>						
Zero	0	144123	0	143389	0	143256
Half	-164	144887	-174	144139	-177	144022
Full	-319	145803	-332	145106	-332	144863

coercivity. The average slope in the tensile direction was -1.63×10^{-3} Oe/ μ strain while in the compressive direction it was -1.54×10^{-3} Oe/ μ strain. The amount of change in the coercivity at maximum strain is approximately the same for both tension and compression, 0.5 Oe for tension versus an average of 0.53 Oe for compression. The coercivity changes also have less scatter.

The actual coercivity as a function of strain is shown in table 6.4. The offset between the tension and compression runs, due to repositioning of the inspection head is present. The stress cycling effect as mentioned in the hysteresis loss discussion is also present. The percent change in the coercivity at maximum strain averages 2.0% in both tension and compression modes. The downward drift with each stress cycle (as seen in the hysteresis loss) is almost nonexistent in the

Table 6.4: Coercivity (in Oe) for rail puller runs

Strain Level	First Run		Second Run		Third Run	
	Strain ($\times 10^{-6}$)	H_c	Strain ($\times 10^{-6}$)	H_c	Strain ($\times 10^{-6}$)	H_c
<u>Tension</u>						
Zero	0	25.70	0	25.52	0	25.49
Half	163	25.40	164	25.27	166	25.28
Full	325	25.11	323	25.03	325	24.98
<u>Compr.</u>						
Zero	0	25.21	0	25.21	0	25.20
Half	-164	25.76	-174	25.44	-177	25.44
Full	-319	25.73	-332	25.71	-332	25.69

coercivity. There was a shift between the first and second runs in the tensile regime, none between the second and third runs and none in any of the compression runs.

Conclusions

Inspection head measurements were successful in monitoring the changes in the hysteresis parameters with applied stress in an actual component of railroad rail. The trends in the parameters were the same as those seen under laboratory conditions. Increasing tension increased the maximum differential permeability and remanence while it decreased the hysteresis loss and coercivity. Increasing compression decreased the maximum differential permeability

and remanence while it increased the hysteresis loss and coercivity. The changes in the maximum differential permeability can be explained on the basis of the theory of Sablik, Jiles, et al, since in a magnetostrictive material such as steel the applied stress contributes an additional term to the anisotropy energy, as discussed in Chapter 1, and this results in the change in permeability.

CHAPTER 7. CONCLUSIONS

It was found that there were definite trends in the hysteresis parameters as tensile stress is increased along the direction of application of the magnetic field. The hysteresis loss and coercivity have been seen to decrease with tensile stress in the elastic range. The remanence and maximum differential permeability have been seen to increase with increasing tensile stress up to the Villari reversal point. These changes with stress were attributed to the contribution of stress to anisotropy as explained by Jiles (8). After mechanical yielding, the trends seen in the parameters reverse. This was attributed to the production of dislocations from the plastic deformation which alters the observed coercivity of the material (7).

The change in the hysteresis parameters with stress in various laboratory specimens were successfully monitored by using an inspection head placed on the surface of the specimens. Increasing tension increased the remanence and the maximum differential permeability while it decreased the hysteresis loss and coercivity. Increasing compression generally decreased the remanence and maximum differential permeability while it increased the hysteresis loss and coercivity. The microstructure of the specimens played a role in determining the rate of change in the magnetic parameters with stress.

Microstructure has been seen to play a major role in determining the magnetic response of a ferromagnetic material. Surface conditions, such as scale and curvature also affected the inspection head measurements because of changes in the flux path.

After comparing a group of laboratory rail specimens with sections of railroad rail of corresponding microstructures, it was found that the relative values of the hysteresis loss and coercivity remained constant. This shows that the transfer of technology from laboratory measurements to field measurements can be achieved by the use of the Magnescope.

Inspection head measurements were successful in monitoring the changes in the hysteresis parameters with applied stress in an actual component of railroad rail. The trends in the parameters were the same as those seen under laboratory conditions. Increasing tension increased the maximum differential permeability and remanence while it decreased the hysteresis loss and coercivity. Increasing compression decreased the maximum differential permeability and remanence while it increased the hysteresis loss and coercivity.

In summary, the magnetic hysteresis technique is capable of monitoring the changes in the hysteresis parameters due to stress. The strength of this method derives principally from its ability to measure several independent parameters independently and the possibility of separating the effects of

stress and microstructure from monitoring these several parameters.

REFERENCES

1. Néel, L., Cahiers de Physique 1944, 25, 21.
2. Williams, H.J., Physical Review 1947, 71, 646.
3. Williams, H.J., Bozorth, R.M., and Shockley, W., Physical Review 1949, 75, 155.
4. Bozorth, Ferromagnetism, D.Van Nostrand Co. Inc., Princeton, New Jersey 1954.
5. Chin, G.Y., and Wernick, J.H., Ferromagnetic Materials, Vol 2, E.P. Wohlfarth (ed.), North-Holland Publishing Co., Amsterdam, 1980, pp. 55-188.
6. Jiles, D.C., Journal of Physics D: Applied Physics 1988 21, 1186.
7. Jiles, D.C., Journal of Physics D: Applied Physics 1988, 21, 1196.
8. Jiles, D.C., Physica Status Solidi (a) 1988, 108, 417.
9. Gorkunov, É.S. and Batukhtina, I.N., Soviet Journal of NDT 1988, 24, 177.
10. Gorkunov, É.S., Somova, V.M. and Buldakova, N.B., Soviet Journal of NDT 1989, 23, 42.
11. Mikheev, M.N. and Gorkunov, E.S., Soviet Journal of NDT 1981, 17, 579.
12. Kwun, H., and Burkhardt, G.L., Journal of Applied Physics 1987, 61, 1576.
13. Thompson, S.M., Allen, P.J. and Tanner, B.K., IEEE Transactions on Magnetics 1990, 26, 1984.
14. Stoner, E.C. and Wohlfarth, E.P., Philosophical Transactions of the Royal Society (London) 1948, A240, 74.
15. Preisach, F., Zeit. Phys. 1935, 94, 277.
16. Jiles, D.C. and Atherton, D.L., Journal of Physics D 1984, 17, 1265.

17. Sablik, M.J., Kwun, H., Burkhardt, G.L. and Jiles, D.C., Journal of Applied Physics 1988, 64 (10), 5402.
18. Pitman, K.C., IEEE Transactions on Magnetics 1991, 26, 1978.
19. Garikepati, P., Chang, T.T., and Jiles, D.C., IEEE Transactions on Magnetics 1988, 24, 2922.
20. Langman, R., NDT International Oct. 81, 255.
21. Langman, R., NDT International 1987, 20, 93.
22. Jiles, D.C., Chang, T.T., Hougen, D.R. and Ranjan, R., Journal of Applied Physics 1988, 64, 3620.
23. Langman, R. IEEE Transactions on Magnetics 1990, 26, 1246.
24. Sanford-Francis, C.H.A., British Journal of NDT 1978, 20, 119.
25. Sanford-Francis, C.H.A., British Journal of NDT 1981, 23, 241.
26. Bussière, J.F. Materials Evaluation 1986, 44, 560.
27. Jiles, D.C. and Atherton, D.L., Journal of Applied Physics 1984, 22, 2115.
28. Brown Jr., W.F., Physical Review 1949, 75, 147.
29. Schneider, C.S. and Semcken, E.A., Journal of Applied Physics 1981, 52, 2425.
30. Jiles, D.C., Hariharan, S., and Devine, M.K., IEEE Transactions on Magnetics 1990, 26, 2577.
31. Eichmann, A., private communication.

ACKNOWLEDGEMENTS

I would like to express my sincerest appreciation to Dr. David C. Jiles, my major professor for his guidance, encouragement, patience (especially when I may forget to bring an inspection head or two), and most of all, for exposing me to the world of magnetism. The push for giving presentations and the opportunities for making contacts with people in the field will always be valued. Your enthusiasm was the driving force behind this work.

I would also like to thank Dr. Otto Buck, Dr. William Lord and Dr. R. William McCallum for serving on my program of study committee. Their advice, comments and experience were most helpful.

Special thanks are also due to David Utrata of the Association of American Railroads for providing many of the samples, and the facilities to perform the research. Your free lunches helped a poor starving graduate student "stay out of trouble" throughout my time here.

I would also like to express my gratitude to my fellow workers at Ames Laboratory, especially Brian Merkle, "Mr. Social Director" and our Magnetism Group. They made the long days (and nights) in the lab pass by quickly

Finally, I would like to thank my family and friends, both here and back in Chicago for their love and unfailing support for this "farm boy" during my graduate study here.

They have been there for both the good and bad times. I count myself fortunate to have such a caring group of supporters.

This work was sponsored by the Center for NDE at Iowa State University and was performed at the Ames Laboratory. Ames Laboratory is operated for the U.S. Department of Energy by Iowa State University under Contract No. W-7405-ENG-82. The United States government has assigned the DOE Report number IS-T 1539 to this thesis.

APPENDIX (Data for Parameter Plots)

Data for Figures 3.3 through 3.7

Applied Stress	Delta Hyst. Loss	Delta Coerc.	Delta Reman.	Delta Max Diff Perm	Delta Max Induct.
Sample AISI 4130					
0.00	0	0.00	0	0	0
80.08	-92	-1.43	1398	523	9
164.38	-874	-3.02	2984	1558	-141
248.68	-2370	-3.81	3523	2159	-157
332.97	-3276	-4.10	3368	2617	-342
404.63	-4709	-4.09	3017	2287	-536
Sample AISI 4140					
0.0	0	0.00	0	0	0
53.1	-918	-1.30	550	142	80
118.0	-1531	-3.06	1430	222	146
151.7	-1453	-3.84	1861	286	195
222.5	-3067	-6.30	3783	434	612
286.6	-4358	-7.34	4607	516	813
475.1	-7561	-7.17	3132	463	67

Data for Figures 4.11 through 4.13

	Applied Stress (MPa)	Delta Reman. (Gauss)	Delta Coerc. (Oe)	Delta Max Diff Perm
W1	-200	-526	0.98	-62
	-100	-291	0.22	-40
	0	0	0.00	0
	100	-96	-0.33	-16
	200	-89	-0.55	-18
W2	-200	-873	1.01	-102
	-100	-488	0.57	-45
	0	0	0.00	0
	200	170	-0.77	-2
W3	-200	-1074	1.78	-132
	-100	-595	1.02	-93
	0	0	0.00	0
	100	243	-0.50	22
	200	391	-0.68	34
W4	-200	-1509	1.34	-159
	-100	-843	0.55	-104
	0	0	0.00	0
	100	158	-0.98	39
	200	235	-0.96	41
W5	-200	-1188	1.60	-115
	-100	-651	0.87	-76
	0	0	0.00	0
	100	37	-1.10	-20
	200	33	-1.39	-1
W6	-200	-578	2.05	-71
	-100	-175	1.31	-22
	0	0	0.00	0
	100	466	-0.11	44
	200	682	-0.30	54

W15

-200	-1241	1.70	-120
-100	-736	0.68	-86
0	0	0.00	0
100	525	-0.24	50
200	864	-1.49	103

W23

-200	-1046	1.03	-90
-100	-594	0.43	-60
0	0	0.00	0
100	-12	-1.15	17
200	27	-1.65	16

CF&I

-200	-1098	1.55	-113
-100	-575	0.74	-52
0	0	0.00	0
100	283	-0.50	30
200	354	-1.05	78